8 Basic Measurements

Measurements in particle and nuclear physics span a wide range of observables, conditions, and collision systems. They may involve the determination of cross section, momentum spectra, angular distributions, particle lifetimes, particle mass, and so on. This chapter introduces several of these types of measurements and observables. We begin, in §8.1, with definitions and commonly used notations used by practitioners of the field and follow up in §8.2 with notions of particle decay and cross section. Measurements of elementary observables such as the momentum and the energy of particles produced in scattering experiments are discussed §8.3 whereas techniques for the identification of long- and short-lived particles are described in §§8.4 and 8.5, respectively. Lastly, §8.6 discusses issues involved in searches and discoveries of new particles and elementary processes.

8.1 Basic Concepts and Notations

8.1.1 Particle Scattering and Definition of Cross Section

The scattering of α-particles off a thin foil of gold (illustrated schematically in Figure 8.1) by H. Geiger and E. Marsden in the early 1910s led E. Rutherford to the discovery of the atomic nucleus and a first estimate of its size. Geiger and Marsden observed that while most of the α-particles were little deflected by their passage through this gold foil, a small but significant fraction was backscattered (i.e., scattered by more than 90^o). Rutherford understood that only a massive object could deflect the charged and heavy alpha particles. He formulated a model based on the Coulomb interaction by which he could predict the number of scattered α as a function of their scattering angle θ relative to their initial direction, and he was able to accurately reproduce the observations of Geiger and Marsden. He thus concluded the existence of a massive and extremely small atomic nucleus. This discovery gave birth to the fields of nuclear and particle physics.

Rutherford relied on a quantitative description of the number of deflected particles, dN, detected in a small solid angle $d\Omega$, as a function of their scattering angle θ, as illustrated in Figure 8.1. In his model, the scattering angle θ is determined by the impact parameter b of the incoming α-particle onto the target nucleus, thereby defining a ring of area $2\pi b\, db$, as shown in Figure 8.2. Classically, this defines the **differential cross section** of the nucleus $d\sigma$ associated with a specific scattering direction

$$\frac{d\sigma}{d\Omega}(\theta) = -\frac{b}{\sin\theta}\frac{db}{d\theta}, \tag{8.1}$$

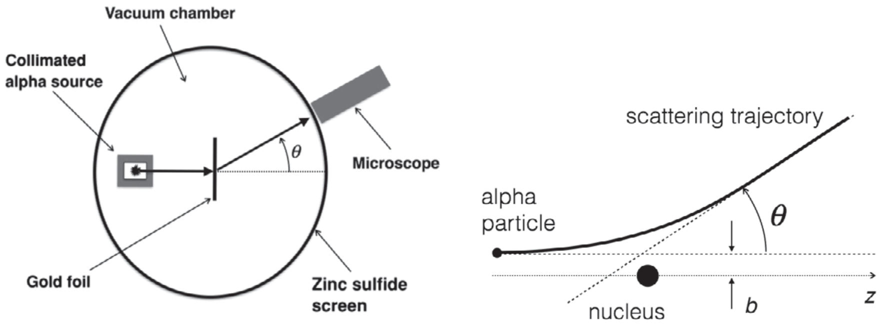

Fig. 8.1 (Left) Schematic of the apparatus used by Rutherford, Geiger, and Marsden to study the scattering of α-particles off a gold foil. (Right) Model formulated by Rutherford to explain the observation of back-scattered particles.

where b is the impact parameter of the collision, θ is the deflection angle of the particle relative to its incident direction, and $d\Omega$ the solid angle in which the particle is measured. For a purely Coulomb (electrostatic) interaction, one has

$$\frac{d\sigma}{d\Omega}(\theta) = \left(\frac{ZZ'e^2}{4E}\right)^2 \frac{1}{\sin^4 \theta/2}, \tag{8.2}$$

where Z and Z' are the atomic number of the colliding nuclei, e the electron charge, and E the kinetic energy of the incoming particle. Integration over all rings $2\pi b\,db$, corresponding to the observation of all scattering angles, leads to the total effective area of the target or **total scattering cross section**.

In a scattering experiment involving a fixed-target and an incoming beam, the number of particles dn deflected in a solid angle $d\Omega$, per unit time, is proportional to the incoming flux N_0 (particles per unit time) of beam particles, the number of target nuclei per unit area,

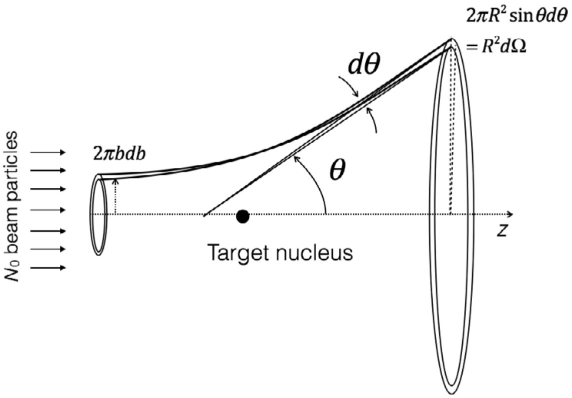

Fig. 8.2 Geometric definition of cross section in the context of Rutherford's model of the scattering of α-particles off gold nuclei.

N/S, and the differential scattering cross section:

$$\frac{dn}{d\Omega} = N_0 \frac{N}{S} \frac{d\sigma}{d\Omega}(\theta, \phi). \tag{8.3}$$

The number of target nuclei per unit area may be written

$$\frac{N}{S} = \frac{\rho t}{A} A_0, \tag{8.4}$$

where ρ is the target material density, t is the physical thickness of the target foil, A is the atomic mass of the material, and A_0 is Avogadro's number. The differential scattering cross section may then be determined by precise measurements of the incoming flux, the target thickness, and the outgoing flux of particles $dn(\theta, \phi)$ in a specific solid angle $d\Omega$ at scattering angle θ relative to the direction of the incoming particle:

$$\frac{d\sigma}{d\Omega}(\theta, \phi) = \frac{1}{N_0} \frac{A}{\rho t A_0} \frac{dn(\theta, \phi)}{d\Omega}. \tag{8.5}$$

The scattering cross section, between a projectile and a target, depends on the nature of the interaction that takes place, as well as the size and internal structure of colliding particles. The Coulomb interaction of two point-like objects leads to a definite and specific angular dependence of the scattering cross section. Deviations from the differential scattering cross section expected from a Coulomb interaction at very large deflection angle and higher collisional energies revealed the existence of an object of finite size within the atom, the nucleus, and eventually enabled study of the nuclear force. Scattering experiments, and more specifically measurements of differential cross sections were thus instrumental in the discovery and study of the atomic nucleus, its structure, the nuclear force, and so on.

The notions of differential and total cross sections are readily extended to all types of elementary collisions, whether elastic or inelastic, and are determined by the number of particles produced at specific angles or momenta relative to the number of incoming projectiles. Given its $1/r^2$ dependence, the total elastic interaction cross section associated with the Coulomb force is infinite for point-like objects. Other types of processes and interactions have different behaviors and accordingly different differential and total cross sections. It is consequently of much interest to measure partial cross sections (both differential and total) associated with specific subprocesses of an interaction between two colliding particles or nuclei. The cross section of a specific process or interaction expresses its effective surface probability and, as such, says much about the nature and strength of the interaction.

It is customary to break down the cross section of elementary processes according to their type and properties, for instance, elastic scattering cross section, diffractive cross section, interaction or inelastic cross section, and so on. It is also common to report cross sections corresponding to specific particle production processes whether exclusive, semi-exclusive, or inclusive. One can, for example, measure the production cross section of pions, kaons, or other particle species, in the context of a specific interaction. By extension, one can also consider how such cross sections depend on the colliding partners (whether protons, neutrons, or nuclei, etc.) and the beam energy. It is also possible to break down cross section measurements in terms of other global collision characteristics such as the (estimated) impact parameter of collisions or the presence/absence of specific particles or other specific features in the final state of interactions.

In closing this section, it is important to remark that the cross section of particular process is a property of that process and should thus be independent of experimental conditions. Evidently, experimental conditions may hinder or alter measurements of this cross section (integral or differential) and it is thus necessary to consider how experimental conditions may affect or alter the outcome of a specific measurement. This very important topic is discussed in detail in Chapter 12.

8.1.2 Relativistic Kinematics

Modern experiments in particle and nuclear physics are commonly carried out at high collisional energies and involve measurements of particles with large momenta. The use of relativistic kinematics is thus usually advised, if not required. In this and the following sections, we use natural units: $c = \hbar = 1$.

In special relativity, and even more so in general relativity, one distinguishes vectors according to their properties of transformation when expressed in two different coordinate systems. Space–time coordinates are denoted with a contravariant four vector with components x^μ:

$$x^\mu = (x^0, x^1, x^2, x^3) \equiv (t, \vec{x}). \tag{8.6}$$

Similarly, the components of the contravariant four momentum of a particle are denoted p^μ:

$$p^\mu = (p^0, p^1, p^2, p^3) \equiv (E, \vec{p}). \tag{8.7}$$

The time-like component p^0 corresponds to the *total* energy of the particle while the space-like components p^1, p^2, p^3 correspond to the momentum components, commonly denoted $\vec{p} = (p_x, p_y, p_z)$.

Many of the problems of interest in nuclear and particle physics involve collisions of beam particles (also called projectiles) onto a fixed target (see Figure 8.6) or collisions of two beams traveling colinearly, but in opposite directions. We thus adopt a right-handed coordinate system with the z-axis, or third component of the momentum vector, corresponding to the beam axis (and direction). In this context, there are three natural and convenient choices of reference frames: the target rest frame, the projectile rest frame, and the center of mass (CM) rest frame. These correspond to reference frames where the target, the projectile, and the CM are at rest, respectively.

Given our choice of z-axis, coordinate transformations between these three frames of reference leave the first and second components of the momentum invariant, while the third component and energy are transformed according to a Lorentz transformation (discussed in the text that follows). It is thus convenient to introduce the notion of **transverse momentum** vector $\vec{p}_T$, defined as

$$\vec{p}_T \equiv (p_x, p_y), \tag{8.8}$$

and its norm (magnitude)

$$p_T = \sqrt{p_x^2 + p_y^2}. \tag{8.9}$$

The four-momentum vector of a particle may thus also be written $p = (E, \vec{p}_T, p_z)$.

We adopt the space–time metric tensor convention $g_{\mu\nu}$, defined as

$$g_{\mu\nu} = g^{\mu\nu} = \begin{pmatrix} 1 & 0 & 0 & 0 \\ 0 & -1 & 0 & 0 \\ 0 & 0 & -1 & 0 \\ 0 & 0 & 0 & -1 \end{pmatrix}. \tag{8.10}$$

The covariant vectors (also called one-form) x_μ and p_μ are related to their contravariant counterparts according to

$$x_\mu = g_{\mu\nu} x^\nu = (t, -x_1, -x_2, -x_3), \tag{8.11}$$

$$p_\mu = g_{\mu\nu} p^\nu = (E, -p_1, -p_2, -p_3), \tag{8.12}$$

where we used the Einstein convention that a repeated index is summed (unless indicated otherwise). Conversely, one also has

$$x^\mu = g^{\mu\nu} x_\nu, \tag{8.13}$$

$$p^\mu = g^{\mu\nu} p_\nu. \tag{8.14}$$

The scalar product of two four-vectors a and b is defined as

$$a \cdot b = a^\mu b_\mu = g_{\mu\nu} a^\mu b^\nu = g^{\mu\nu} a_\mu b_\nu. \tag{8.15}$$

In particular, the modulus of the four momentum vector p is written

$$p^2 = p \cdot p = p_o^2 - p_1^2 - p_2^2 - p_3^2 = E^2 - |\vec{p}|^2 = m^2, \tag{8.16}$$

where we introduced the mass m of the particle (recall that we are using natural units in which $c = 1$).

8.1.3 Lorentz Transformation

A Lorentz transformation along the beam axis leaves the transverse momentum invariant. Consider the momentum, $p = (E, \vec{p}_T, p_z)$, of a particle in a reference frame K (e.g., the target rest frame). The components $p' = (E', \vec{p}_T{}', p_z{}')$ in a frame K' (e.g., projectile rest frame) moving along $+z$ at a velocity β relative to K are written

$$E' = \gamma(E - \beta p_z), \tag{8.17}$$

$$\vec{p}_T{}' = \vec{p}_T, \tag{8.18}$$

$$p_z{}' = \gamma(p_z - \beta E), \tag{8.19}$$

where $\gamma = (1 - \beta^2)^{-1/2}$.

Transformations for motion along x- or y-axes are trivially obtained by substitution of the appropriate momentum components. Transformations for motion along an arbitrary direction,[1] $\hat{\beta}$, at velocity β, requires one explicitly separates the momentum components parallel and perpendicular to $\hat{\beta}$. One writes

$$\vec{p} = \vec{p}_T + \vec{p}_\parallel, \tag{8.20}$$

with

$$\vec{p}_\parallel = (\vec{p} \cdot \hat{\beta})\hat{\beta}, \tag{8.21}$$

$$\vec{p}_T = \vec{p} - \vec{p}_\parallel. \tag{8.22}$$

The $\vec{p}_T$ component is unmodified by the transformation along $\hat{\beta}$, but the parallel component is boosted according to

$$|\vec{p}_\parallel\,'| = \gamma \left(|\vec{p}_\parallel| + \beta E\right). \tag{8.23}$$

The boosted moment can consequently be written

$$\vec{p}\,' = \vec{p} + \left[(\gamma - 1)\vec{p} \cdot \hat{\beta} + \gamma E\right] \hat{\beta}. \tag{8.24}$$

8.1.4 Rapidity

Equation (8.16) reduces the number of degrees of freedom of a free particle from four to three. Given the invariance of $\vec{p}_T$ relative to Lorentz transformations along the beam axis (z), one can regard Eq. (8.16) as introducing a special connection between the energy and the z-component of the momentum. In this context, it is convenient to introduce the notion of particle rapidity, noted y, and defined according to

$$y = \frac{1}{2} \ln \left(\frac{E + p_z}{E - p_z}. \right) \tag{8.25}$$

The rapidity is by construction a dimensionless quantity, and it can be either positive, negative, or null. In the nonrelativistic limit, $v \approx 0$, it is equal to the velocity in units of the speed of light (see Problem 8.1), thereby providing a justification for the name "rapidity."

While y is not an invariant under Lorentz transformations, one finds its transformation law is particularly simple. Consider, for instance, the rapidity of a particle in frame K' introduced in Eq. (8.25):

$$y' = \frac{1}{2} \ln \left(\frac{E' + p_z{}'}{E' - p_z{}'} \right), \tag{8.26}$$

---

[1] Breaking with earlier chapters where the caret indicates statistical estimators, the caret is used here to denote unit vectors.

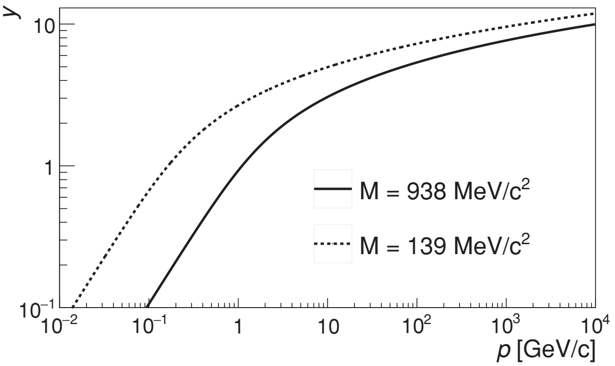

Fig. 8.3 Beam rapidity as a function of the momentum of beam particles plotted for protons (solid line) and pions (dashed line).

and substitute the expressions for E' and p_z' from Eq. (8.17).

$$y' = \frac{1}{2}\ln\left(\frac{\gamma(E-\beta p_z)+\gamma(p_z-\beta E)}{\gamma(E-\beta p_z)-\gamma(p_z-\beta E)}\right), \tag{8.27}$$

$$y' = \frac{1}{2}\ln\left(\frac{1-\beta}{1+\beta}\times\frac{E+p_z}{E-p_z}\right), \tag{8.28}$$

$$y' = y - \frac{1}{2}\ln\left(\frac{1+\beta}{1-\beta}\right), \tag{8.29}$$

$$y' = y - y_\beta, \tag{8.30}$$

where in the last line, we introduced the rapidity of the moving frame K' relative to K, noted y_β. The simplicity of this transformation relation makes it very convenient for transformation of the particle kinematics between the target, projectile, and CM rest frames.

The rapidity of particles propagating along the z-axis (e.g., $p = p_z$, the beam axis) is plotted in Figure 8.3 as a function of their momentum p.

8.1.5 Pseudorapidity

Experimentally, the determination of the rapidity of a particle requires that one identifies its mass. But as we will see later in this chapter, although it is relatively straightforward to measure the momentum of a particle (or its energy), it is not always possible to measure both quantities directly or to readily identify the species of the particle detected. Thus, the masses of detected particles are often unknown, and calculation of their rapidity from, say, measured momenta, is consequently not feasible. Fortunately, there is a convenient substitute, known as **pseudorapidity**, defined according to

$$\eta = -\ln\left(\tan(\theta/2)\right), \tag{8.31}$$

where θ is the polar angle between the particle momentum $\vec{p}$ and the beam axis. It is easy to verify (see Problem 8.3) that η equals y in the limit where the mass of a particle is negligible compared to its energy, that is, for $m << E$.

Evidently, in the limit $m = 0$, which hold for (real) photons, one has (in natural units)

$$E = p \tag{8.32}$$

$$m_T = p_T, \tag{8.33}$$

and consequently

$$y = \eta. \tag{8.34}$$

8.1.6 Useful Kinematic Relations

The energy and momentum of a particle of known mass may be expressed in terms of its velocity, $\vec{\beta} = \vec{v}/c$, according to (in natural units)

$$E = \gamma m, \tag{8.35}$$

$$\vec{p} = \gamma m \vec{\beta}, \tag{8.36}$$

with the Lorentz factor $\gamma = (1 - \beta^2)^{-1/2}$. The velocity, β, can consequently be determined from the ratio

$$\beta = \frac{|\vec{p}|}{E}. \tag{8.37}$$

It is useful to introduce the notion of **transverse mass**:

$$m_T = \sqrt{p_T^2 + m^2}. \tag{8.38}$$

One may then express the energy and the *longitudinal* (or z) component of the momentum of a particle in terms of y and m_T, as follows (see Problem 8.4):

$$E = m_T \cosh y, \tag{8.39}$$

$$p_z = m_T \sinh y. \tag{8.40}$$

Alternatively, one may also obtain the modulus of the momentum $|\vec{p}|$ and the z-component based on the transverse momentum p_T and the pseudorapidity (see Problem 8.7):

$$|\vec{p}| = p_T \cosh \eta, \tag{8.41}$$

$$p_z = p_T \sinh \eta. \tag{8.42}$$

Measurements of momentum components are commonly carried out in terms of *spherical coordinates* (p, θ, ϕ), defined in Figure 8.4. The momentum components (p_x, p_y, p_z) may then be obtained with the following relations:

$$p_x = p_T \cos \phi, \tag{8.43}$$

$$p_y = p_T \sin \phi, \tag{8.44}$$

$$p_z = p \cos \theta, \tag{8.45}$$

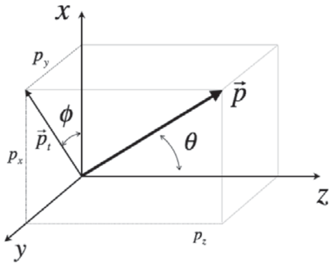

Fig. 8.4 Definition of spherical coordinates relative to the beam direction (z-axis).

where $p_T = p \sin\theta$. The angles are obtained with the relations

$$\phi = \tan^{-1}(p_y/p_x), \tag{8.46}$$

$$\theta = \tan^{-1}(p_T/p_z). \tag{8.47}$$

8.1.7 Mandelstam Variables

The Mandelstam variables, denoted s, t, and u, were introduced by Stanley Mandelstam in 1958. They are defined in the context of nuclear collisions involving two incoming and two outgoing particles, with four momenta denoted p_1, p_2, p_3, and p_4 as illustrated in Figure 8.5:

$$s = (p_1 + p_2)^2 = (p_3 + p_4)^2, \tag{8.48}$$

$$t = (p_1 - p_3)^2 = (p_2 - p_4)^2, \tag{8.49}$$

$$u = (p_1 - p_4)^2 = (p_2 - p_3)^2, \tag{8.50}$$

where the right-hand side equalities are determined by virtue of energy and momentum conservation. By construction as squares of four-momentum sums or differences, the three variables s, t, and u are Lorentz invariants and thus have the same value in all reference frames.

The variable s is particularly useful to quantify the collision energy. For instance, in fixed-target geometry, one has $p_1 = (E_1, \vec{p}_1)$, and $p_2 = (m_2, 0)$. One then gets

$$s = (E_1 + m_2)^2 - p_1^2 = m_1^2 + m_2^2 + 2E_1 m_2, \tag{8.51}$$

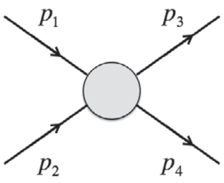

Fig. 8.5 The Mandelstam variables s, t, and u are defined based on the four-momenta p_1, p_2, p_3, and p_4 as shown. The circle represents an energy and momentum conserving interaction between two incoming particles with 4-momenta p_1 and p_2, and producing two particles with momenta p_3, and p_4.

which is proportional to the beam energy E_1. On the other hand, in symmetric collider geometry, that is, with colliding beams of equal momentum but opposite directions, one has $p_1 = (E, \vec{p})$ and $p_2 = (E, -\vec{p})$, thereby yielding

$$s = (E + E)^2 - (\vec{p} - \vec{p}) = 4E^2, \tag{8.52}$$

which is proportional to the square of the beam energy. In symmetric collider geometry, the CM is at rest relative to the laboratory. All the energy of the incoming beams is consequently available in the CM frame of the collision. In contrast, in fixed-target geometry the CM is moving toward the target with a velocity $\beta_{CM} = |\vec{p}_{1,\text{lab}}|/(E_{1,\text{lab}} + m_2)$. Only a small fraction of the beam energy is therefore available in the CM frame of the collision. Considering that the acceleration of high-energy beams is an energy-intensive and costly endeavor, it is thus advantageous to collide particles in a collider geometry to maximize the usefulness of the beam energy delivered toward interactions and particle production.

Mandelstam variables are particularly useful also in the calculation of scattering amplitudes because they are frame independent. The variable t, in particular, determines the momentum transferred to particle 3 by the collision.

Finally, note that the tree variables s, t, and u are not independent, and are, in fact, constrained by the relation

$$s + t + u = m_1^2 + m_2^2 + m_3^2 + m_4^2. \tag{8.53}$$

8.1.8 Basic Classifications of Scattering Experiments

Research conducted in the last half century has involved a wide range of collisional energies, beam particles, and target materials. Experiments can be broadly divided into **fixed-target** and **collider geometry** experiments. Fixed-target experiments involve accelerated beams consisting of specific particle species and transport of these beams to bombard a fixed target, which may consist of a "thin" foil or a gas contained in a special vessel. Collider experiments require the acceleration of two beams brought to collide in a colinear geometry, moving in opposite directions (clockwise and counterclockwise). Existing colliders typically use two concentric acceleration/storage rings. The beams intersect and collide at one or more crossing points along the rings, as illustrated in Figure 8.7. Colliders are said to operate in symmetric collider mode if the two beams being accelerated consist of identical particle species (as well as particle and antiparticle combinations, e.g., e^+e^-, $p\bar{p}$) at the same energy. They are said to be asymmetric if the two beams have different energies. It is also possible to produce asymmetric colliding systems, such as $p + Pb$ or $d + Au$.

Huge advances have been realized since the modest beginnings of early accelerators that produced protons and alpha particles of a few MeV. Past and existing facilities were developed to accelerate a wide variety of beams, including electrons, protons, light and heavy stable nuclei, radioactive nuclei with very short half-lives, as well as elementary

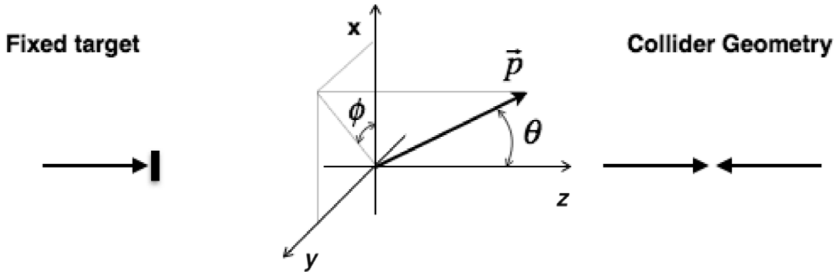

Fig. 8.6 Illustration of the collision geometry of fixed-target and collider mode experiments.

particles such as pions or muons. Figure 8.8 presents a summary of trends in accelerators at facilities worldwide since the 1930s.

Collisions between two elementary particles (or nuclei) can be broadly divided into elastic and inelastic interactions. Elastic collisions, as the name suggests, are nondissipative and involve the deflection of the incoming particles only. At low energy, proton on proton (p + p) inelastic collisions involve the excitation of one or both colliding particles

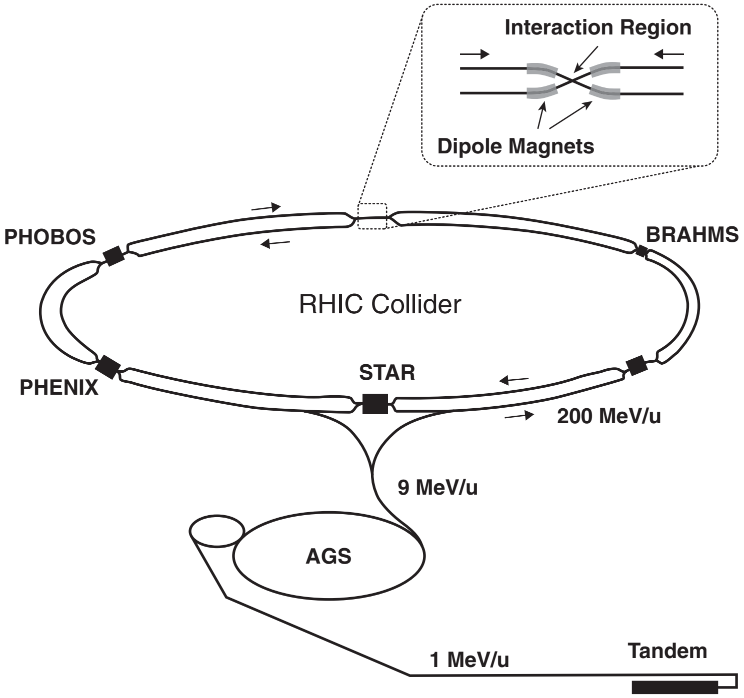

Fig. 8.7 Schematic of the BNL/RHIC collider geometry. Beams traveling counterclockwise (CCW) and clockwise (CW) are tuned to collide at marked intersections points.

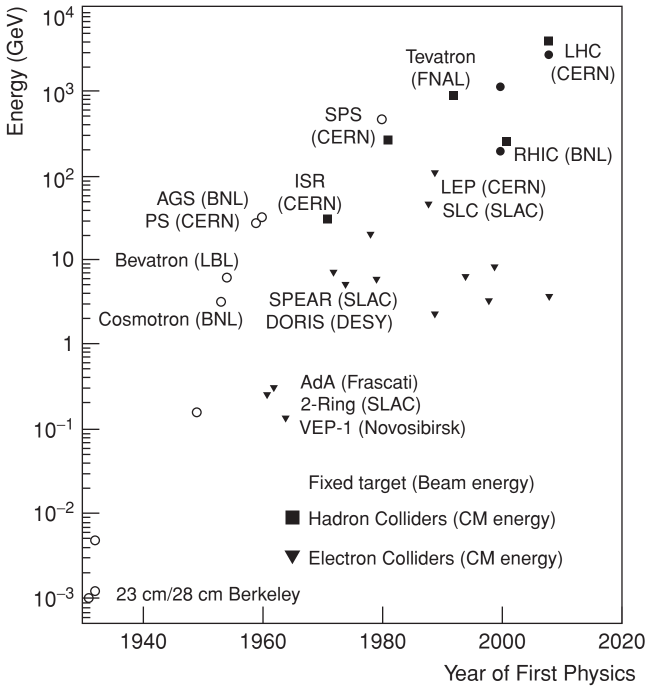

Fig. 8.8 Trend in accelerator energies. Open and solid symbols show fixed-target and collider facilities, respectively, since 1935.

and typically lead to the production two or more particles. At higher energy, p + p collisions produce several tens or even hundreds of particles, while head-on heavy-ion collisions may produce several thousands. Diffractive p + p collisions are inelastic collisions involving a modest energy dissipation and momentum transfer between the colliding partners. One or both of the protons are produced in an excited state from which they decay by emission of one or several hadrons. Such interactions are said to be singly and doubly diffractive depending on whether only one or both protons end up in an excited state and produce particles. Nondiffractive inelastic collisions involve substantial energy dissipation and typically the production of large particle multiplicities (number of particle produced).

It is useful to classify produced particles according to their source. For instance, particles produced by the breakup of the projectile, a process known as beam fragmentation, are observed at rapidities near the projectile rapidity, y_P, and are said to be part of the **projectile fragmentation region**. Likewise, particles found near the target rapidity, y_T (e.g., $y_T \sim 0$ in fixed-target geometry or $y_T \sim -y_P$ in a symmetric collider mode) are commonly associated with the **target fragmentation region**, whereas particles produced in between these two extremes, particularly those around the CM rapidity, y_{CM}, are said to be part of the **central rapidity region**. Clearly, the gap between the projectile and target rapidities grows with increasing beam energy. At Relativistic Heavy-Ion Collider (RHIC) top heavy-ion energy, $\sqrt{s_{NN}} = 200$ GeV, the beams have rapidities of ±5.3, while at CERN, the

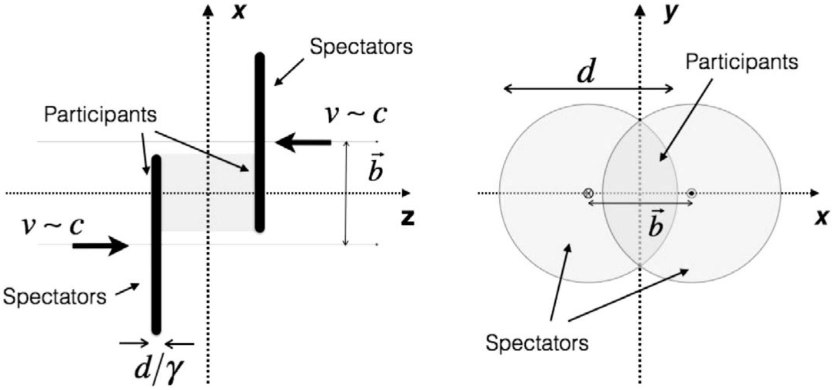

Fig. 8.9 Longitudinal (left) and transverse (right) profiles of two heavy-ion nuclei shortly before a collision at relativistic ($\beta \sim c$) energy. The diameter d of the nuclei is Lorentz contracted by a factor γ in the beam direction. The light gray area between the nuclei (longitudinal profile) is where most of the particle production takes place after the nuclei have passed through each other.

7 TeV proton beams have a rapidity of ±9.6. Observations indicate that projectile and target fragmentation produce particles clustered within approximately one unit of rapidity of the projectile and target rapidity, respectively. The central rapidity region thus spreads considerably with increasing beam energy. This means that at large beam energies, it is rather challenging to design and build detector systems capable of measuring all three regions, and experiments are consequently designed to focus on only particular aspects of the particle production. For instance, detectors such as STAR, PHENIX at RHIC, DO, and CDF at the Tevatron, and CMS, ATLAS, and ALICE at the LHC are best equipped to measure the central rapidity region, whereas TOTEM and LHCf at the LHC were designed to study the production of “forward” particles.

In the context of heavy-ion collisions, one can further extend this source classification based on the impact parameter of the collision between two nuclei. Figure 8.9 schematically illustrates the longitudinal and transverse profiles of two large nuclei colliding with an impact parameter b. In the longitudinal profile, the nuclei are represented in the CM reference frame (assuming a symmetric collision) just before the collision. They appear as thin slices because their longitudinal size is contracted by the Lorentz factor $\gamma = (1 - \beta^2)^{-1/2}$, with β being their velocity in the CM frame. In the transverse profile, the nuclei are represented as they pass through one another. At collider energies, the nuclei have speeds approaching the speed of light. The penetration time (measured in the CM frame) is thus of the order of $d/\gamma c$, with d being the diameter of the nuclei. At RHIC top energy, this amounts to $\sim 4 \times 10^{-25} s$, or 0.12 fm/c. On the other hand, transverse propagation of a signal from one side (for instance, the top of the transverse profile in Fig. 8.9) to the other side (the bottom) of a nucleus requires a minimum of $\sim$ 12 fm/c. In the transverse plane, one can consequently divide the colliding nuclei into two regions, as illustrated in Figure 8.9. The darker shade region, consisting of the two nuclei overlapping area, is

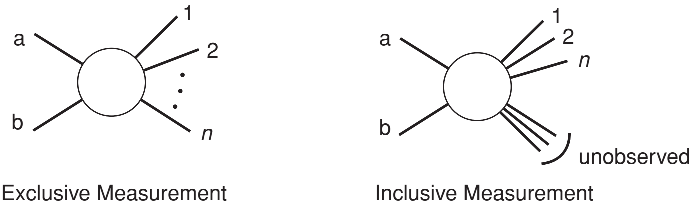

Fig. 8.10 Exclusive measurements involve all particles produced whereas semiexclusive and inclusive measurements specify only a small fraction of the final state of collisions (or decays).

directly and instantly affected by the collision. Nucleons in this region are thus called **participants**. Their interactions may produce particles at all rapidities, that is, in both the central rapidity region and the beam/target fragmentation regions. Nucleons in the lighter shaded areas of the two nuclei are referred to as spectators. Signals that nucleons of the participant region have undergone interactions with another nucleus do not reach them until well after the two nuclei have passed through one another. These nucleons are therefore not directly involved in the main part of the interaction and can thus indeed be considered spectators. The two colliding nuclei are completely shattered, but the spectator nucleons continue their path forward/backward at the beam/target rapidity. They lead to particle production in the beam/target fragmentation regions. Particle produced by the participants, typically deemed of more interest, dominate the central rapidity region.

Experiments can be further classified according to the type of measurements they carry (Figure 8.10). Measurements are said to be exclusive if they involve the totality of produced particles. Such measurements were possible in the early days of particle physics with, for instance, bubble chamber detectors. However, modern experiments conducted at high-beam energy typically do not cover all regions of particle production and thus cannot measure all produced particles (charged or neutral). They are consequently called semi-exclusive or inclusive. In an inclusive measurement, only one or a few of the produced particles are detected and their properties (e.g., momentum, species type, and so forth) measured. The final state of a collision thus cannot be completely specified or identified.

8.2 Particle Decays and Cross Sections

8.2.1 Particle Decays

The decay of an elementary particle of mass M and four-momentum $p = (E, \vec{p})$ is a stochastic phenomena determined by an exponential distribution (§3.5)

$$P(t) = \frac{1}{\gamma\tau} \exp\left(-\frac{t}{\gamma\tau}\right), \tag{8.54}$$

where τ is the **proper lifetime** of the particle determined by the **decay rate** Γ,

$$\tau = \hbar/\Gamma, \tag{8.55}$$

and $\gamma = E/M$. The function $P(t)$ gives the probability the particle lives for a time t or greater before decaying. For a particles with n decay channels, the rate Γ is the sum of the partial decay rates Γ_i corresponding to each of the decay channels:

$$\Gamma = \sum_{i=1}^{n} \Gamma_i. \tag{8.56}$$

The partial decay rate of a particle of mass M into n particles, in its rest frame, is given by

$$d\Gamma = \frac{(2\pi)^4}{2M} |\mathfrak{M}|^2 \, d\Phi_n(P; p_1, ..., p_n), \tag{8.57}$$

where $|\mathfrak{M}|$ represents the amplitude of the decay process. The factor $d\Phi_n$ is an element of n-body phase space equal to

$$d\Phi_n(P; p_1, ..., p_n) = \delta^4\left(P - \sum_{i=1}^{n} p_i\right) \prod_{i=1}^{n} \frac{d^3 p_i}{(2\pi)^3 2E_i}, \tag{8.58}$$

where the delta function $\delta^4(P - \sum_{i=1}^{n} p_i)$ encapsulates energy conservation between the parent and decay particles. It is useful to note that the n-body phase space factor $d\Phi_n$ can be calculated recursively

$$\begin{aligned} d\Phi_n(P; p_1, ..., p_n) = {} & d\Phi_j(P; p_1, ..., p_j) \\ & \times d\Phi_{n-j+1}(P; q, p_{j+1}, ..., p_n)(2\pi)^3 dq^2, \end{aligned} \tag{8.59}$$

where

$$q^2 = \left(\sum_{i=1}^{j} E_i\right)^2 - \left(\sum_{i=1}^{j} \vec{p}_i\right)^2. \tag{8.60}$$

Two-Body Decays

In the rest frame of a particle of mass M, a two-body decay yields $\vec{p}_1 = -\vec{p}_2$. Energy conservation implies $M = E_1 + E_2$. One thus finds

$$E_1 = \frac{M^2 - m_2^2 + m_1^2}{2M}, \tag{8.61}$$

$$= \frac{\left[(M^2 - (m_1 + m_2)^2)(M^2 - (m_1 - m_2)^2)\right]^{1/2}}{2M}, \tag{8.62}$$

from which we conclude

$$d\Gamma = \frac{1}{32\pi^2} |\mathfrak{M}|^2 \frac{|p_1|}{M^2} d\Omega, \tag{8.63}$$

where $d\Omega = d\phi_1 d(\cos\theta_1)$ is the solid angle within which particle 1 is emitted. Experimentally, M^2 can be obtained from the invariant mass $(p_1 + p_2)^2$ of the pair and thus provides a basis for short-lived particle reconstruction and identification (see §8.5).

Three-Body Decays

In the rest frame of a three-body decaying particle of mass M, momentum conservation constrains the momenta $\vec{p}_1$, $\vec{p}_2$, and $\vec{p}_3$ of the produced particles to lie in the same (decay) plane. Energy conservation further constrains the energy of the three particles, and one has

$$m_{12}^2 = (P - p_3)^2 = M^2 + m_3^2 - 2ME_3, \tag{8.64}$$

where we defined $m_{ij}^2 = p_{ij}^2$ with $p_{ij} = p_i + p_j$. Additionally, one has

$$m_{12}^2 + m_{13}^2 + m_{23}^2 = M^2 + m_1^2 + m_2^2 + m_3^2. \tag{8.65}$$

One can then write the decay rate as

$$d\Gamma = \frac{1}{16M(2\pi)^5} |\mathfrak{M}|^2 \, dE_1 dE_2 d\alpha d(cos\beta) d\gamma, \tag{8.66}$$

where α, β, and γ represent three Euler angles defining the orientation of the decay plane. The decay rate may also be written (see Problem 8.10)

$$d\Gamma = \frac{1}{16M(2\pi)^5} |\mathfrak{M}|^2 \, |p_1^*||p_3| dm_{12} d\Omega_1^* d\Omega_3, \tag{8.67}$$

where $|p_1^*|$ and $d\Omega_1^*$ represent the momentum and solid angle of emission of particle 1 in the rest frame of particles 1 and 2, while $d\Omega_3$ is the angle of the third particle in the rest frame of the decaying particle. The momenta $|p_1^*|$ and $|p_3|$ are given by

$$|p_1^*| = \frac{\left[(m_{12}^2 - (m_1 + m_2)^2)(m_{12}^2 - (m_1 - m_2)^2)\right]^{1/2}}{2m_{12}}, \tag{8.68}$$

$$|p_3| = \frac{\left[(M^2 - (m_{12} + m_3)^2)(M^2 - (m_{12} - m_3)^2)\right]^{1/2}}{2M}, \tag{8.69}$$

For angular momentum $J = 0$ decaying particles, or averaging over all spin states of a $J \neq 0$ particle, the rate simplifies to

$$\begin{aligned} d\Gamma &= \frac{1}{8M(2\pi)^3} \overline{|\mathfrak{M}|^2} dE_1 dE_2, &(8.70)\\ &= \frac{1}{8M(2\pi)^3} \overline{|\mathfrak{M}|^2} dm_{12}^2 dE_{23}^2, &(8.71) \end{aligned}$$

which provides a basis for Dalitz plots (see §8.5.2).

8.2.2 Cross Section Measurements

Invariant Cross Section

Because the longitudinal momentum component, p_z, of produced particles is reference-frame dependent, the expression of the differential cross section is also reference-frame dependent. It is thus useful to seek an expression for the cross section in terms of a relativistic invariant. Given $E^2 = m^2 + p_T^2 + p_z^2$, and for fixed p_T, one gets $EdE = p_z dp_z$. A longitudinal boost of the differential dp_z thus yields

$$\begin{aligned} dp_z{}^* &= \gamma\left(dp_z - \beta dE\right) = \gamma\left(dp_z - \beta\frac{p_z}{E}dp_z\right), \\ &= \gamma\frac{dp_z}{E}\left(E - \beta p_z\right) = \frac{dp_z}{E}E^*, \end{aligned} \tag{8.72}$$

from which we find that $dp_z{}^*/E^* = dp_z/E$. Since p_T is invariant under a longitudinal boost, we thus conclude that d^3p/E is a Lorentz invariant. One can thus express cross sections in a frame-independent way using the invariant cross section

$$E\frac{d^3\sigma}{dp^3} = E\frac{d^3\sigma}{d\phi p_T dp_T dp_z}, \tag{8.73}$$

$$= \frac{d^2\sigma}{\pi dp_T^2 dy}, \tag{8.74}$$

where, in the second line, we used the fact that $dp_z/E = dy$ and averaged over ϕ.

As stated earlier, it is not always possible to identify the species or type of detected particles. It is thus convenient to also define cross section in terms of the pseudorapidity variable η. At a fixed or given p_T, one writes

$$\frac{dN}{d\eta} = \frac{dN}{dy}\frac{dy}{d\eta}. \tag{8.75}$$

The derivative $dy/d\eta$ is calculated at fixed p_T as follows:

$$\frac{dy}{d\eta} = \frac{dy/dp_z}{d\eta/dp_z} = \frac{p}{E} = \sqrt{1 - \frac{m^2}{m_T^2\cosh^2 y}}. \tag{8.76}$$

The differential cross section may thus be written

$$\begin{aligned} \frac{dN}{d\eta dp_T} &= \sqrt{1 - \frac{m^2}{m_T^2\cosh^2 y}}\frac{dN}{dydp_T}, \\ &= \sqrt{1 - \left(1 + p_T^2/m^2\right)^{-1}\cosh^{-2}y}\frac{dN}{dydp_T}. \end{aligned} \tag{8.77}$$

The Jacobian $J = \sqrt{1 - \left(1 + p_T^2/m^2\right)^{-1}\cosh^{-2}y}$, illustrated in Figure 8.11 as a function of y for selected values of the ratio p_T/m, tends to unity for $p_T \gg m$. It may thus be neglected when the mass of particles are very small compared with the energy or momentum scale of the process.

n-Body Cross Section

The **exclusive** differential cross section of a collision producing n particles (illustrated in Figure 8.12) may be written as

$$d\sigma = \frac{(2\pi)^4\,|\mathfrak{M}|^2}{4\sqrt{(p_1\cdot p_2)^2 - m_1^2m_2^2}}d\Phi_n(p_1 + p_2; p_3, ..., p_n + 2), \tag{8.78}$$

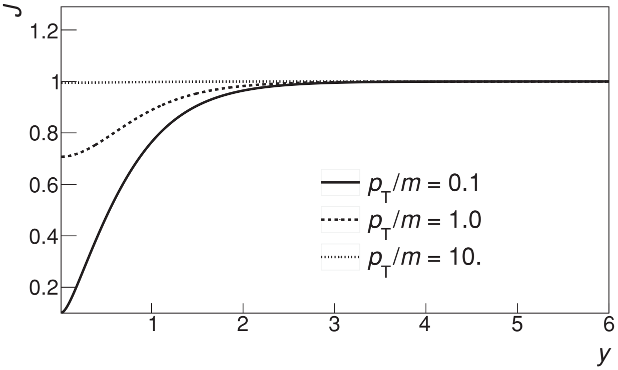

Fig. 8.11 Jacobian $J = \partial y/\partial\eta$ for selected values of the ratio p_T/m.

with

$$d\Phi_n = \delta^{(4)}\left(\vec{P} - \sum_{j=1}^{n}\vec{p}_j\right)\prod_{i=1}^{n}\delta\left(p_i^2 - m_i^2\right)d^4p_i, \tag{8.79}$$

where $|\mathfrak{M}|$ represents the amplitude of the scattering process and Φ_n is a phase space factor defined by Eq. (8.58). In the rest frame of m_2 (the lab frame), one has $p_1 = (E_1, \vec{p}_1)$ and $p_2 = (m_2, 0)$, which yields

$$\sqrt{(p_1 \cdot p_2)^2 - m_1^2 m_2^2} = m_2 p_1. \tag{8.80}$$

In the center-of-mass frame, $p_1 = (E_1, \vec{p}_{1,\mathrm{cm}})$ and $p_2 = (E_2, -\vec{p}_{1,\mathrm{cm}})$, Eq. (8.80) becomes

$$\sqrt{(p_1 \cdot p_2)^2 - m_1^2 m_2^2} = p_{1,\mathrm{cm}}\sqrt{s}. \tag{8.81}$$

Two-Body Reactions

Cross sections for two-body processes are conveniently expressed in terms of the Mandelstam variable t defined in Eq. (8.48):

$$\frac{d\sigma}{dt} = \frac{1}{64\pi s}\frac{1}{|p_{1,\mathrm{cm}}|^2}|\mathfrak{M}|^2 \tag{8.82}$$

In the CM frame, one has

$$t = (E_{1,\mathrm{cm}} - E_{3,\mathrm{cm}})^2 - p_{1,\mathrm{cm}}^2 - p_{3,\mathrm{cm}}^2 + 2p_{1,\mathrm{cm}}p_{3,\mathrm{cm}}\cos\theta_{\mathrm{cm}}, \tag{8.83}$$

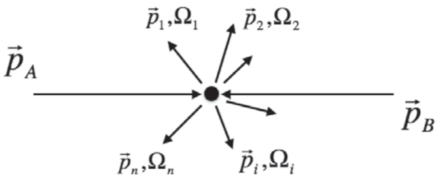

Fig. 8.12 Differential cross section of an n-body process.

where $\theta_{\rm cm}$ is the angle of emission, in the CM frame, relative to the direction of particle 1. Since $\cos u = 1 - 2\sin^2 u/2$, one gets

$$t = (E_{1,\rm cm} - E_{3,\rm cm})^2 - (p_{1,\rm cm} - p_{3,\rm cm})^2 - p_{1,\rm cm}p_{3,\rm cm}\sin^2\theta_{\rm cm}/2. \tag{8.84}$$

For $2 \to 2$ scatterings, limiting values for t_0 and t_1, corresponding to $\theta_{\rm cm} = 0$ and $\theta_{\rm cm} = \pi$ respectively, are given by (see Problem 8.8):

$$t_0(t_1) = \left[\frac{m_1^2 - m_3^2 - m_2^2 + m_4^2}{2\sqrt{s}}\right]^2 - (p_{1,\rm cm} \mp p_{3,\rm cm})^2. \tag{8.85}$$

Luminosity

In a fixed-target experiment, the rate of interactions of a specific type, hereafter noted W_i, is proportional to the flux of incoming beam particles, F, the total number of target particles, N_T, and the cross section, σ_i, of the process, so that

$$W_i = \sigma_i N_T F, \tag{8.86}$$

where the rate W_i has units of inverse time, $[T^{-1}]$, the number of targets has units of inverse area $[L^{-2}]$, and the flux has units of inverse time $[T^{-1}]$. In contrast, in a collider experiment, there is no "solid target," one must then replace the product of the number of target nuclei (per unit area) and the flux of incoming particles by a beam parameter known as **instantaneous luminosity**, L. The measured rate is thus

$$W_i = \sigma_i L, \tag{8.87}$$

where L has units of inverse area, inverse time $[T^{-1}L^{-2}]$.

The time-integrated luminosity multiplied by the cross section yields the number of observable interactions, N_i, of a given type over the life of an experiment:

$$N_i = \sigma_i \int L\,dt. \tag{8.88}$$

The luminosity L delivered by a collider depends on the number of beam particles, the frequency of beam crossings, as well as beam focusing according to

$$L = \frac{nfB_1B_2}{A} \tag{8.89}$$

where n is the number of beam bunches, f the revolution frequency, B_1 and B_2 are the number of beam particles contained per bunch, and A is the cross-sectional area of the overlapping crossing beams. While the number of bunches n, and the frequency f are typically fixed by an **accelerator's design**, the parameters B_1, B_2, and A are functions of the **accelerator tuning** and may thus vary over time. Since tuning an accelerator is an intricate and complex task, accelerator facilities typically begin their existence with small delivered luminosities. However, as beam physicists master the operation of their machine, they generally raise the delivered luminosity to eventually achieve **design luminosity** within weeks or months of operation.

The design luminosity of a machine is limited by various conditions, including the maximum number of bunches, maximum number of ions per bunch, and focusing. The LHC was originally designed to achieve a luminosity of 10^{34} cm^{-2}s^{-1}. The total interaction cross section of proton–proton collisions is of the order of 60 mb (6×10^{-26} cm^2) at LHC energy. This makes for an interaction rate of about 6×10^8 s^{-1} or 600 MHz.

Given a process cross section σ_i, the number of observable interactions N_i is intrinsically limited by the integrated luminosity $\int L\,dt$ (as well as the efficiency of the measurement). Accelerator facilities thus typically report *delivered* integrated luminosities in terms of the inverse of cross section units. For instance, an integrated luminosity of one inverse picobarn corresponds to the minimal luminosity required to observe (on average) one event with a cross section of one picobarn, while an integrated luminosity of one inverse femtobarn, which is one thousand times larger, corresponds to the minimal integrated luminosity needed to observe a one femtobarn process. Laboratories also customarily report plots of the delivered integrated luminosity as a function of (operation) time as an indicator of the performance of their accelerator facilities.

8.2.3 Measurements of Differential Cross Sections

Differential measurements of cross section may be carried out for single or multiple particles concurrently. Whether one wishes to obtain differential cross sections as a function of transverse momentum, p_T, rapidity, y, or other kinematic variables, it is necessary to scan a dataset and fill one or several histograms corresponding to the kinematic variables and particles of interest. One uses one-dimensional histograms (§4.6) for differential quantities with dependency on a single variable and multidimensional histograms (§4.6.3) for cross sections involving several kinematic variables, several particles, or both.

Consider, as an example, the determination of the transverse momentum differential cross section for the production of charged particles in A + A collisions. Let us assume one has a dataset consisting of a known number of events, N_{ev}, satisfying some event conditions and data **quality criteria** (commonly called **quality cuts**). The dataset must then be scanned for all events satisfying the event condition and quality criteria of interest. Each event is itself scanned for particles, with appropriate particle selection and quality selection criteria. Each particle satisfying the selection criteria produce entries in a p_T histogram, $H_{p_T}(i)$, in bin i determined by the momentum of the particle and the partition of the histogram (i.e., its minimum and maximum value boundaries and the number of bins). A raw differential spectrum S_{p_T} is obtained by scaling the histogram by the number of events included in the dataset scan. That is, for each bin i, one calculates

$$S_{p_T}(i) = \frac{1}{N_{\text{ev}}} H_{p_T}(i), \tag{8.90}$$

where N_{ev} is the actual number of events satisfying the event selection and quality selection criteria. One obtains an estimator of the particle density $\hat{\rho}_1(p_T) = dN/dp_T = \sigma^{-1} d\sigma/dp_T$ as function of p_T by further dividing $S_{p_T}(i)$ by the bin width, $\Delta p_{T,i}$, of each bin i:

$$\hat{\rho}_1(p_T) \equiv dN/dp_T = \frac{S_{p_T}(i)}{\Delta p_{T,i}}, \tag{8.91}$$

$$= \frac{1}{N_{ev}\Delta p_{T,i}} H_{p_T}(i). \tag{8.92}$$

Technically, the quantity $\hat{\rho}_1(p_T)$ obtained with this formula is "still" a histogram. To obtain an actual function, one must account for bin width averaging, as discussed in §12.3.5. Additionally, various instrumental conditions typically limit the efficiency of the measurement and introduce p_T smearing effects, as well as backgrounds. Techniques to correct for such effects are presented in §12.3.1. Neglecting such effects, or assuming they have been properly accounted for, one obtains the differential cross section by dividing the density $\rho_1(p_T)$ by the luminosity $\mathcal{L}$ integrated by the experiment and the event selection efficiency ε:

$$d\sigma/dp_T = \frac{1}{\mathcal{L}\varepsilon}\rho_1(p_T). \tag{8.93}$$

Techniques and issues related to the evaluation and correction of instrumental inefficiencies are discussed in §12.3.1.

The aforementioned procedure can be readily extended for differential cross section measurements involving two or more kinematical variables. For instance, one obtains the density $\rho_1(\eta, p_T)$ by filling a two-dimensional histograms with the particles pseudorapidity η and transverse momentum p_T:

$$\hat{\rho}_1(\eta, p_T) \equiv \frac{d^2N}{d\eta dp_T} = \frac{1}{\sigma}\frac{d\sigma}{d\eta dp_T} = \frac{S_{\eta,p_T}(i)}{\Delta\eta_i \Delta p_{T,i}}, \tag{8.94}$$

$$= \frac{1}{N_{ev}\Delta\eta_i \Delta p_{T,i}} H_{\eta,p_T}(i, j), \tag{8.95}$$

where the indices i and j span bins in pseudorapidity and transverse momentum, respectively. The double differential density $d^2\sigma/d\eta dp_T$ is obtained, as for single differential cross section, by dividing by the integrated luminosity $\mathcal{L}$ and event efficiency. The procedure is similar for two- or multiparticle cross sections, except that one must then scan each event for pairs, triplets, or n-tuplets of particles, as appropriate. This involves two, three, or more, nested loops over all particles of each event. The number of pairs and triplets scale as $n(n-1)$ and $n(n-1)(n-2)$, respectively. The process can thus become particularly CPU-intensive and fastidious for very large multiplicity events such as those produced in high-energy nucleus nucleus collisions at RHIC or LHC. However, note that for indistinguishable particles, it is unnecessary to examine all pairs (triplets or n-tuplets). For pairs, one can use a loop over all particles of the event for the first particle, that is, $i = 1, \ldots, n$, while the loop for the second particle is restricted to $j = i + 1, \ldots, n$. Subsequently, one must then appropriately symmetrize the histograms used to evaluate two-particle densities.

8.3 Measurements of Elementary Observables

Studies of interest in nuclear and particle physics include measurements of total and differential cross sections, correlation functions, particles mass and lifetimes, and much more. At their very core, all these measurement involve elementary measurements of particle momentum, energy, production angles, and so on. We discuss basic measurement techniques

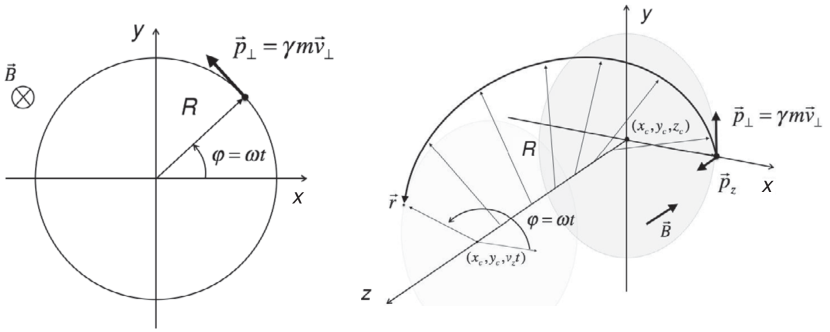

Fig. 8.13 (Left) Principle of measurement of particle momenta with a magnetic spectrometer. (Right) illustration of helicoidal trajectories described by Eqs. (8.98–8.100).

in this section and describe more advanced techniques in remaining section of this Chapter as well as in Chapters 10 and 11. Several data correction techniques are presented in Chapter 12.

8.3.1 Momentum Measurements

The momentum of a particle can be measured by observing its trajectory under the influence of a force of known magnitude and direction. For charged particles, this can be readily accomplished with static electric or magnetic fields. Here, we focus our discussion on magnetic spectrometers, which are far more common than electric field based momentum analyzers.

A charged particle, q, traveling in a magnetic field $\vec{B}$ at speed $\vec{v}$ is deflected by the Lorentz force, which acts as a centripetal force. The particle thus follows (in the absence of other forces) a helicoidal path of radius R such that

$$|\vec{F}_{\text{Lorentz}}| = kq|\vec{v} \times \vec{B}| = kqv_T B = \frac{mv_T^2}{R}, \tag{8.96}$$

for v_T perpendicular to $\vec{B}$. We then conclude that the particle momentum transverse to the field (as illustrated in Figure 8.13) is given by

$$p_T = kqBR, \tag{8.97}$$

where $k = 0.3$ when the charge q is expressed in unit charge (e.g., ± 1), the momentum p_T in GeV, the magnetic field B in Tesla, and the trajectory radius R in meters. For a uniform magnetic field oriented along the z-direction, the momentum component p_z is a constant, and the trajectory may be described parametrically as a helicoidal trajectory

$$x(t) = x_c + R\cos(\omega t + \phi_0), \tag{8.98}$$

$$y(t) = y_c + R\sin(\omega t + \phi_0), \tag{8.99}$$

$$z(t) = z_c + v_z t, \tag{8.100}$$

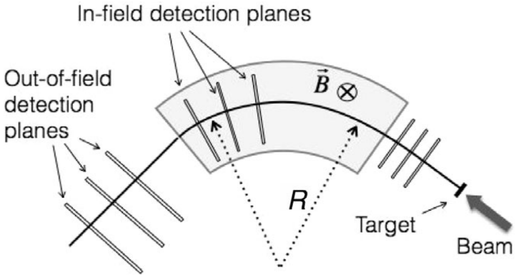

Fig. 8.14 Particle momentum determination with a dipole magnetic spectrometer.

where the coordinates (x_c, y_c) represent the center of the circular path and z_c is the position of the particle along the z-axis at $t = 0$. The particle's angular velocity is

$$\omega = \frac{v_T}{R} = \frac{p_T}{mR} \tag{8.101}$$

and the pitch λ of the helicoidal trajectory depends on the ratio of the momentum components parallel and transverse to the magnetic field

$$\tan\lambda = \frac{p_z}{p_T}. \tag{8.102}$$

Reconstruction of the momentum of a particle can be achieved by detecting the trajectory of the particle $\vec{r}(t)$ and evaluating its radius R and pitch angle λ. Equation (8.97) provides the magnitude p_T while Eq. (8.102) enables the determination of p_z. The magnitude of the momentum is thus $p = \sqrt{p_T^2 + p_z^2}$.

The determination of the trajectory $\vec{r}(t)$ is typically accomplished using position-sensitive sensors, discussed in §8.3.3, and requires sophisticated pattern recognition techniques to identify the charged particle trajectories measured by these sensors. Examples of these techniques are discussed in Chapter 9.

Charged Particles Detection and Tracking

Several magnetic field and detector geometries are commonly used to carry out magnetic analysis of particle momenta, including dipole, solenoidal, and toroidal field configurations. A plurality of detector technologies have been developed to measure charged particle trajectories within these field configurations and determine momenta and identify particle species. Detector technologies much in use include scintillator slats, straw tube chambers, wire chambers, pad chambers, time projection chambers, as well as solid-state detectors such as pixel detectors, strip detectors, or silicon drift detectors. Detectors may be placed either within or outside the field region, as schematically illustrated in Figure 8.14. A full discussion of tracker topologies and associated technologies is well beyond the scope of this textbook. We thus limit our discussion to few illustrative examples of the methods used in charged particle detection with a solenoidal field configuration (Figure 8.15).

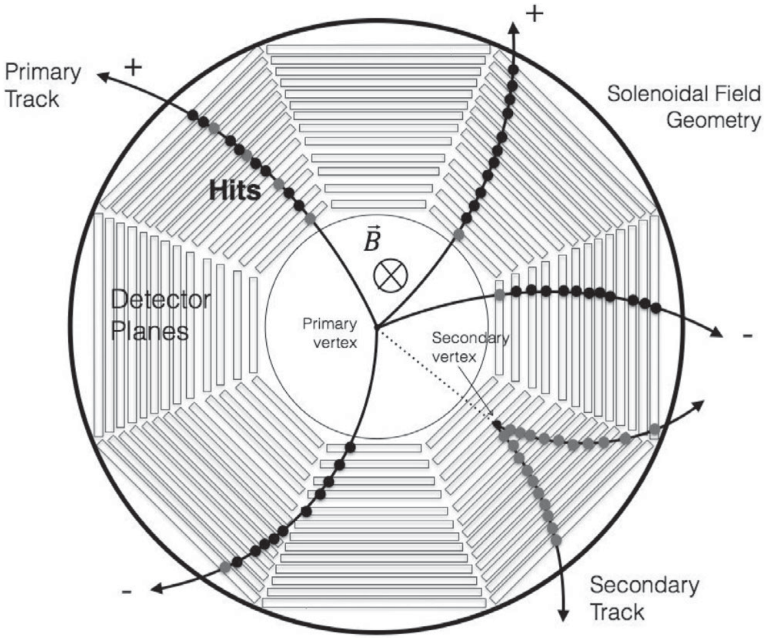

Fig. 8.15 Charged particle detection in a multilayer charged particle detector within a solenoidal field configuration. Open rectangles represent detector layers and solid dots represent energy deposition "hits" within these layers. Solid lines represent primary charged particle tracks, whereas the dotted line represents a neutral short-lived particle that decayed into two charged particles within the detector volume.

High-momentum charged particles passing through matter lose energy via interactions with (mostly) electrons of the medium. Electronic excitations resulting from these interactions can be exploited toward ionization of the medium or light emission (fluorescence). Tracking detectors are thus designed to either detect the presence and position of ionization or light emission within a specific detection plane or volume. A combination of several detection planes, as illustrated in Figure 8.15, then yield **hits** that provide an "image" or snapshot of the particle trajectory called **track**. Tracking detectors measure the position and energy deposited at these hits. Pattern recognition software can then be used to find series of hits that belong to a given track, and the curvature and trajectory of each track are used to determine the momentum of the particles as per Eq. (8.97). Extrapolation of the trajectories to their point of origin then yields the momentum vector of the particles at their point of production, called **production vertex** or just **vertex**.

Tracks may be fitted for momentum vector determination with or without the inclusion of their production vertex position. Tracks reconstructed and fitted without the inclusion of the primary vertex are often known as **global tracks**, whereas those fitted with the primary vertex are loosely called primary tracks, although they may, technically, originate from unresolved secondary decays taking place near the primary vertex. Such unresolved secondary tracks constitute a systematic background in the determination of particle production cross sections and correlation functions.

A wide variety of pattern recognition techniques are commonly used to reconstruct hits, tracks, and production vertices. We here limit our discussion to some of the most basic techniques in Chapter 9 and refer the interested reader to specialized works [18, 41, 42, 43, 60, 86, 88, 89, 94, 95, 102, 127, 139, 178].

Tracks are usually classified based on their vertex of origin and mechanism of production. Tracks originating from the main collision vertex, known as a **primary vertex**, are called **primary tracks**, while those produced by decays of long-lived particles (e.g., K_s^0, Λ^0) are called **secondary tracks** and are associated with a **secondary vertex**, as illustrated in Figure 8.15. Tracks produced within the detection apparatus by particle interactions with detector materials may be referred to as **tertiary** or **background tracks**.[2] Tracks obtained by wrong or accidental associations of hits are generally known as **faked tracks** or **ghost tracks**. It is important to realize that secondary tracks are a byproduct of the scattering process under study and cannot be avoided. Measurements of the production cross section of the short-lived particle decays that produce secondary tracks are actually of interest to fully characterize the scattering processes under study. Tertiary and ghost tracks, however, are detector artifacts and thus ought to be minimized by careful design of the tracking system and the software used in the reconstruction of the data. This calls for detection systems that reduce the amount of materials that can cause tertiary tracks. It also requires the number of tracking planes be optimized to reduce ambiguities in the extrapolation and extension of tracks. Also note that minimization of materials reduces **Multiple Coulomb Scattering** (MCS), which otherwise limits the achievable momentum resolution (see discussion that follows).

Momentum Resolution

The magnetic fields used in magnetic spectrometers are typically quite stable and measured with very high precision. The momentum resolution achieved in measurements is thus almost entirely determined by tracking resolution and more specifically by the resolution δC of the track curvature C defined as the multiplicative inverse of the radius R. Fluctuations of the curvature are driven by process noise consisting predominantly of MCS and measurement noise associated with the spatial or hit resolution (RES) of measuring devices (discussed in §8.3.3)[3]:

$$\delta C^2 = \delta C_{\text{res}}^2 + \delta C_{\text{MCS}}^2. \tag{8.103}$$

Let us first examine the term δC_{res} dependent on position resolution. At a minimum, three position measurements are required to estimate the radius of a circular trajectory, as illustrated in Figure 8.16a. The center of the circle is readily obtained by finding the intersection of segment bisectors S_1 and S_2. Let us define midpoints $\vec{r}_A = \vec{r}_1 + \Delta\vec{r}_{12}/2$ and $\vec{r}_B = \vec{r}_2 + \Delta\vec{r}_{23}/2$, with $\Delta\vec{r}_{12} = \vec{r}_2 - \vec{r}_1$ and $\Delta\vec{r}_{23} = \vec{r}_3 - \vec{r}_2$. The bisectors may be written $\Delta\vec{r}_{AC} = \vec{r}_A - \vec{r}_C$ and $\Delta\vec{r}_{BC} = \vec{r}_B - \vec{r}_C$, with $\vec{r}_C$ defining the position of the center of the

---

[2] Note that background tracks are often referred to as secondary tracks also.

[3] In a wider context, C_{res} is known as measurement noise while C_{MCS} corresponds to process noise. These concepts are discussed in §12.1.

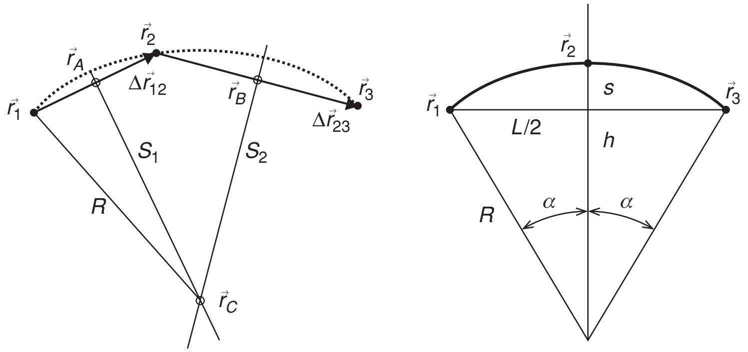

Fig. 8.16 (a) Determination of a track center and *f* radius. (b) Definition of the track sagitta *s*.

circle. By definition of the bisectors, one has

$$\Delta\vec{r}_{12} \cdot \Delta\vec{r}_{AC} = 0, \tag{8.104}$$

$$\Delta\vec{r}_{23} \cdot \Delta\vec{r}_{BC} = 0, \tag{8.105}$$

which reduces to

$$\Delta\vec{r}_{12} \cdot \vec{r}_C = \frac{1}{2}\left(r_1^2 - r_2^2\right), \tag{8.106}$$

$$\Delta\vec{r}_{23} \cdot \vec{r}_C = \frac{1}{2}\left(r_2^2 - r_3^2\right). \tag{8.107}$$

These two equations can be solved (see Problem 8.11) for the components $\vec{r}_C = (x_c, y_c)$. The radius R of the circle is then

$$R = \sqrt{(\vec{r}_1 - \vec{r}_C) \cdot (\vec{r}_1 - \vec{r}_C)}. \tag{8.108}$$

In order to estimate the curvature resolution based on the position resolution, consider the diagram shown in Figure 8.16b, which defines the **track sagitta** $s = x_2 - (x_1 + x_3)/2$ in terms of three position measurements. For a track length L much smaller than the radius, $L << R$, one has

$$s = R(1 - \cos\alpha) \approx R\frac{\alpha^2}{2}. \tag{8.109}$$

Introducing the momentum of the track transverse to the field, and noting $L \approx R\alpha$, one obtains

$$s \approx \frac{R^2\alpha^2}{2R} = \frac{qBL^2}{8p_T}. \tag{8.110}$$

The transverse momentum can then be expressed in the terms of the length of the track L and its sagitta s:

$$p_T = \frac{qBL^2}{8s}. \tag{8.111}$$

Assuming all three measurements have the same position resolution σ_x, and with $L >> s$, the momentum resolution δp is thus entirely determined by the resolution on the sagitta.

For a measurement involving three hits, each with a position resolution σ_x, one gets $\sigma_s = \sqrt{3/2}\sigma_x$. The relative momentum resolution is

$$\frac{\delta p_T}{p_T} = \frac{\sigma_s}{s} = \sqrt{96}\sigma_x \frac{p_T}{qBL^2}. \tag{8.112}$$

The momentum resolution can of course be improved by carrying out N uniformly distributed measurements of the track trajectory. Assuming all measurements have the same resolution σ_x, one finds [150]

$$\frac{\delta p_T}{p_T} = \frac{\sigma_s}{s} = \sqrt{\frac{720}{N+4}}\sigma_x \frac{p_T}{qBL^2}. \tag{8.113}$$

One thus concludes that the relative momentum uncertainty $\delta p/p$ is proportional to the position resolution σ_x and grows linearly with the particle momentum, inversely as the strength of the field B and inversely as the square of the measured track length. There is thus an interest in carrying out momentum measurements with large magnetic fields and large spectrometer enabling large path lengths L determined with very high precision σ_x.

The momentum resolution is also affected by MCS, which amounts to a process noise. Its impact on the relative momentum uncertainty can be estimated as

$$\frac{\delta p_T}{p_T} = \frac{13.6\sqrt{X/X_0}}{qBL}, \tag{8.114}$$

where X/X_0 is the material thickness expressed in units of radiation lengths X_0 [35].

In practice, the usable field strength is limited by the smallest momentum one wishes to detect. Indeed, if the field is very high, low p_T tracks end up having very small radii and may not be measurable. The resolution σ_x is determined by the technologies employed. Drift chambers (wire) have resolutions in the range 50–200 μm, whereas Si pixel and Si strip detectors can achieve resolutions down to a few microns.

The momentum resolution of modern complex detectors is commonly estimated based on Monte Carlo simulations of track propagation and reconstruction involving a detailed description of all detector components and materials, as well as simulators of the sensor responses and resolution. It may also be studied using cosmic rays and the reconstruction of decaying particles with a very narrow (or very well known) decay width (§8.5).

Track Quality Characterization

Not all reconstructed tracks have the same quality. Indeed, various instrumental effects may degrade and smear the quality of tracks randomly. Fortunately, several parameters may be used to assess the quality of reconstructed tracks and reject tracks of lesser quality. Quality criteria common to most reconstruction techniques and experiments include the track χ^2, the number of hits on a track, and the track's distance of closest approach to the primary collision vertex (or secondary vertex in the case of secondary tracks). It is in general possible to carry out analyses with quality criteria that are tailored to the needs of a specific physics analysis.

The track χ^2 is defined as

$$\chi^2 = \sum_{i=1}^{n} \left(\vec{r}_i - \vec{f}_i(x_i|\hat{\theta})\right)^T \mathbf{V}_i^{-1} \left(\vec{r}_i - \vec{f}_i(x_i|\hat{\theta})\right), \tag{8.115}$$

where $\vec{r}_i = (y_i, z_i)$, $i = 1, \ldots, n$, are measured hit positions, $\mathbf{V}_i = \text{Cov}[y_i, z_i]$, and $\vec{f}_i(x_i)$ is the position predicted by the model representing the track in terms of fit parameters $\hat{\theta}$. Fit parameters include the momentum (or track curvature) and angles of emission of the track. If the measurements y_i and z_i can be considered Gaussian deviates and yield a well-calibrated covariance matrix $\mathbf{V}$, the χ^2 values obtained for genuine tracks can be characterized by a χ^2 distribution (see §3.13). It is then possible to use the track χ^2 as a reliable and predictable quality criterion to identify and eliminate bad tracks. Indeed, one can select a maximum χ^2_{max} value and reject all tracks that exceed this criterion with a well-defined selection criterion efficiency given by

$$\varepsilon = \int_0^{\chi^2_{\text{max}}} f_{\chi^2}(z; n)\, dz, \tag{8.116}$$

where $f_{\chi^2}(z; n)$ is the χ^2 distribution for n degrees of freedom given by Eq. (3.163). A track χ^2 thus nominally constitutes a robust, reliable, and well-defined quality selection criterion. In practice, however, the determination of hit errors is often met with considerable challenges, and a proper and precise assessment of the size and correlations of the errors may not be possible. Although a χ^2 may still be used to reject tracks, the efficiency (or losses) associated with a particular maximum χ^2 value may no longer be obtained from Eq. (8.116) but must instead be determined by means of Monte Carlo or embedding techniques (see §12.4.6).

The number of found hits associated with a track, n_F, also provides powerful control of the quality of tracks, particularly when compared to the total number of "possible" hits, n_{max}, that could be on the track given its specific geometry, that is, the number of active sensors (detection planes) physically traversed by the track. Given a particular sensor technology, one expects there is a finite probability ε_{Hit} for finding hits produced by a particular track. For illustrative purposes, let us assume this efficiency is identical for all tracking planes and independent of kinematical track parameters. Let us further assume that the probability of finding a track hit on a particular plane is independent of the probability of finding one on other planes. The probability of finding n_F hits on a track with a possible maximum of n_{max} may then be modeled with a binomial distribution (§3.1):

$$P_B(n_F|n_{\text{max}}, \varepsilon_{\text{Hit}}) = \frac{n_{\text{max}}!}{n_F!(n_{\text{max}} - n_F)!} (\varepsilon_{\text{Hit}})^{n_F} (1 - \varepsilon_{\text{Hit}})^{n_{\text{max}} - n_F}. \tag{8.117}$$

This is illustrated in Figure 8.17 for selected values of efficiencies ε_{Hit} and a maximum value $n_{\text{max}} = 150$.

Because the number of hits actually detected on a track affects the momentum resolution, it is desirable to impose a minimum number of hits, N_{min}, requirement on reconstructed tracks. One must, however, realize that for fixed hit efficiency and number of detector layers, the number of hits detected will then influence the track reconstruction efficiency,

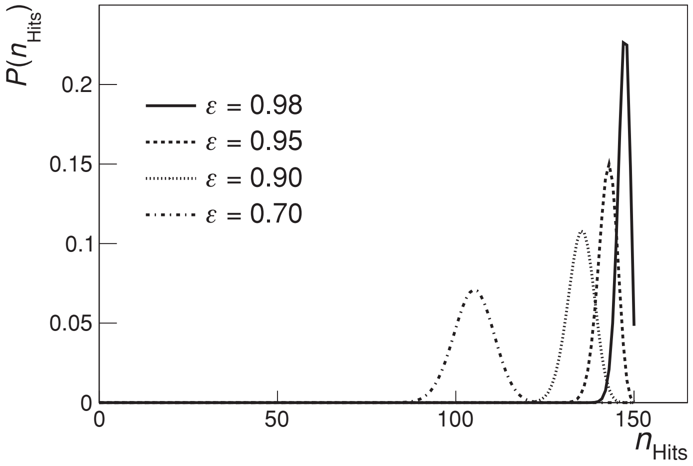

Fig. 8.17 Probability distribution of the number of hits, $n_{\rm Hits}$, associated with reconstructed tracks modeled according to a binomial distribution with selected hit-finding efficiencies ε, and for a maximum number of hits $n_{\rm max} = 150$.

which amounts at best[4] to

$$\varepsilon_{\rm Track}(\varepsilon_{\rm Hit}) = \sum_{n_F=n_{\rm min}}^{n_{\rm max}} P_B(n_F|n_{\rm max}, \varepsilon_{\rm Hit}), \tag{8.118}$$

and is shown in Figure 8.18 as a function of the hit-finding efficiency $\varepsilon_{\rm Hit}$ for selected values of $N_{\rm min}$. Since short tracks are expected to yield inferior momentum resolution and wider distance of closest approach (DCA) distributions, and are also more likely to consists of faked tracks, it is legitimate to require tracks to have a specific minimum number of hits. Equation (8.118) nominally determines the efficiency of the selection criterion (requirement). However, several additional factors may influence the likelihood of adding a found hit to a track. The hit-finding efficiency used in the preceding formula should thus obviously include all these effects.

A selection criterion on the number of hits is particularly useful to eliminate **split tracks**, that is, charged particle trajectories that for one reason or another are reconstructed as two or more track segments rather than a single track. Inclusion of split tracks in measurements leads to overestimation of the particle production cross section as well as spurious features in correlation functions. Fortunately, one can greatly reduce the double counting associated with split tracks by requiring that tracks accepted in an analysis feature a ratio $n_F/n_{\rm max}$ larger than 50%. Indeed, requiring a minimum length of 50% ensures the longest split track segment is utilized while shorter segment(s) are eliminated. One can optionally use a higher ratio requirement (e.g., 60%) if there is a concern that spurious hits may randomly be added to split tracks.

---

[4] This expression accounts only for hit-finding efficiency; other effects may reduce the track-finding efficiency also.

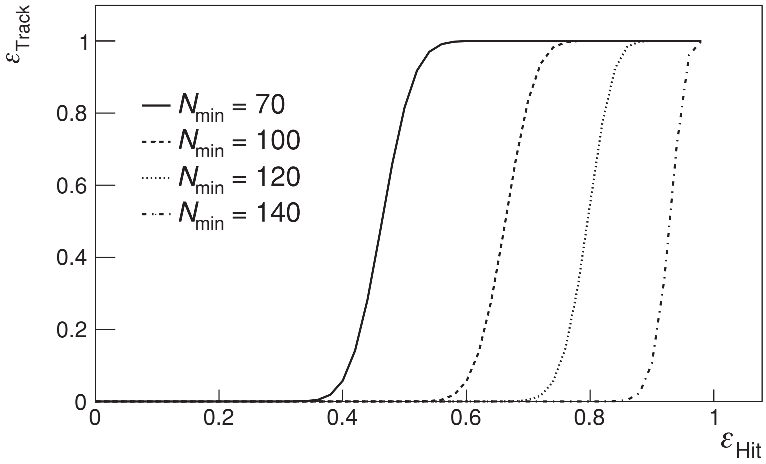

Fig. 8.18 Track-finding efficiency as a function of the hit-finding efficiency for selected values of the minimum of hits requirement N_{min}, assuming a binomial hit-finding distribution and $n_{\mathrm{max}} = 150$.

In practical analyses, it is often the case that the hit-finding efficiency may vary from one detection plane/sensor to the next. It may also depend on the track parameters, and more specifically on the energy deposition of the track determined by the momentum of the track and the angle at which it crosses a specific detection plane. It is also the case that various detector components may malfunction intermittently or become completely nonoperational. An exact calculation of the probability of the track-finding efficiency as determined by hit-finding efficiencies may thus become impractical. Experimenters commonly resort to estimations of track-finding efficiency based on Monte Carlo simulation of the detector performance or embedding techniques (§12.4.6).

The DCA to the collision primary vertex, defined in Figure 8.19, is yet another track parameter routinely used to assess the quality of tracks. It may be expressed as a single quantity or broken into two components, one along the beam axis, and one in the plane transverse to the beam axis. Track DCAs are particularly useful to distinguish primary, secondary, and background tracks. Indeed, secondary and tertiary tracks are produced either by decays or interactions throughout the detector. They are thus unlikely to project

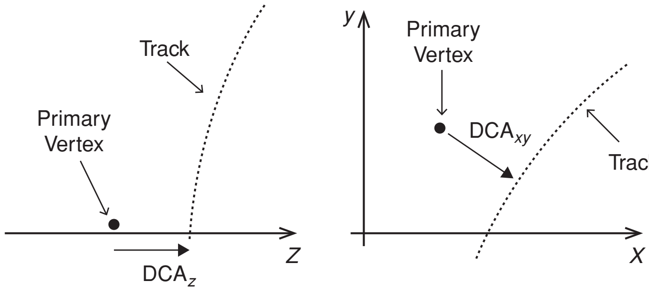

Fig. 8.19 Definition of the distance of closest approach (DCA) to the primary vertex.

back to the primary vertex. A measurement of DCA thus nominally provides an indicator of the origin of the track: secondary or tertiary tracks are expected to have large DCA, while primary tracks should have null DCA.

In practice, finite resolution of hit reconstruction and MCS lead to finite resolution in momentum and angle determination. Primary tracks projected to the main vertex thus have a finite DCA also. The width of the primary track DCA distribution depends on the vectoring resolution and is typically a function of the track momentum and rapidity. It is of course determined largely by the position resolution of the tracking detectors used to identify the tracks. The discrimination of secondary tracks is complicated by the fact that short-lived particles decay stochastically on a time scale determined by their mean life τ. For instance, kaon-short (K_s^0) have a mean life of $(8.954 \pm 0.004) \times 10^{-11}$ s and travel a mean distance $c\tau = 2.69$ cm at the speed of light before decaying. The probability of decaying on a shorter distance is, however, finite. In practice, this means that the secondary particles produced by a decay may look as if they were produced very near the primary vertex. Since primary tracks have a finite width DCA distribution, it becomes strictly impossible, for small DCA values, to distinguish whether a particle is a true primary or actually a secondary. One must then carry out a statistical analysis to determine the likelihood of secondary particles being reconstructed and identified as primary particles (and reciprocally).

Short-lived particles have typically a much smaller production cross section, and secondary tracks thus constitute a small background to primary tracks. It is in fact often sufficient to eliminate secondary tracks on the basis of DCA selection criteria in the longitudinal and transverse directions. The use of specific maximum DCA selection criteria obviously implies losses of primary particles (efficiency) and contamination by secondary particles. One expects the DCA resolution to be determined by MCS effects as well as by the detector granularity and hit precision. The DCA width is thus typically largest at the lowest track momenta and decreases with increasing momentum. It eventually rises, however, when the track curvature is small relative to the position resolution of the detector. Understanding primary track losses and contamination by secondaries is thus typically a nontrivial task best accomplished on the basis of Monte Carlo simulations.

It is also worth pointing out that the track χ^2, the number of hits on a track, and the DCA are typically highly correlated because all three parameters depend on the momentum resolution. The efficiency associated with selection criteria on the χ^2, the number of hits n_F and the DCA thus cannot be represented by a product of three independent efficiencies. Monte Carlo and embedding techniques are thus best for estimating losses and contamination effects.

8.3.2 Calorimeters and Energy Measurements

Calorimeters are devices designed to measure the total energy of particles produced in elementary collisions. They involve complete absorption of particle energy by means of either hadronic or electromagnetic processes. As such, calorimeters tend to be rather bulky and massive. As for tracking devices, several types of calorimeters have been developed and tailored toward various kinds of applications. One generally distinguishes between electromagnetic and hadronic calorimeters.

Electromagnetic and Hadronic Calorimeters

Electromagnetic calorimeters are designed and optimized to measure the energy of leptons (i.e., photons and electrons) by means of electromagnetic interactions. For instance, high-energy electrons penetrating through matter lose energy by scattering and by emission of radiation in the form of photons called *bremsstrahlung radiation*. High-energy photons, in turn, interact through matter via photoelectric effect, Compton scattering, or pair production. These processes lead to the production of electron and photons that also interact with the medium bulk and thereby produce a large flurry of particles known as an **electromagnetic shower**.

Hadronic calorimeters are optimized for the detection of high-energy hadrons but are also generally sensitive to electromagnetic energy. They rely on hadronic interactions of hadrons (e.g., protons, neutrons, pions, etc.) within the bulk material. These interactions produce large numbers of charged and neutral pions. Neutral pions decay and initiate electromagnetic showers, while charged pions have further hadronic interactions that develop into a mixed shower of hadrons and leptons.

Calorimeters are commonly characterized in terms of the e/h ratio, which measures their relative response to leptons and hadrons. A calorimeter is said to be perfectly **compensated** if it features a ratio $e/h = 1$, which means it is equally sensitive (with same gain) to both hadrons and leptons.

Calorimeters are built either with a single and homogeneous material or a combination of absorbing and sensing (shower sampling) materials. **Homogeneous calorimeters** rely on the same material for both the initiation of showers and the production of signals. They usually consist of inorganic crystals (e.g., lead-glass) transparent to light and are read out either by photomultiplier tubes or photodiodes. As such they provide a poor response to hadron and are thus used as electromagnetic calorimeters exclusively.

Sampling calorimeters are typically constructed with alternating layers of absorbing and sampling materials. Absorber materials commonly used include high-density, large atomic number (Z) materials such as lead, tungsten, or uranium. The sampling material may be solid or liquid and chosen to either transmit light (e.g., plastic scintillators) or electric currents (e.g., liquid argon, liquid krypton).

Calorimeters may also be segmented into cells and modules both longitudinally and transversely. Not too common, longitudinal segmentation enables measurements of the longitudinal shape and depth of showers. It may then be used to discriminate hadronic from electromagnetic showers, or high-energy electrons from photons. Transverse segmentation, on the other hand, is used almost universally because it enables measurements of the position (direction) of produced particles based on energy sharing between calorimeter cells.

Electromagnetic showers have a shape and depth that fluctuates within comparatively narrow limits and feature an overall scale determined by the radiation length of the materials composing the calorimeter. Hadronic interactions have smaller cross sections than electromagnetic processes. Hadronic showers thus exhibit larger shower shape fluctuations both transversely and longitudinally. They typically start at a depth determined by the interaction length of the material but their size do not have a simple dependence on the interaction length and are partly determined by the radiation length of the material.

Although calorimeters do not typically contain or stop muons, they are nonetheless sensitive to energy deposition by these particles.

Bolometric Calorimeters

Bolometric calorimeters measure incoming energy fluxes based on the change in temperature ΔT they produce. Assuming the incoming flux is entirely converted into heat, the temperature rise amounts to the ratio of incoming energy by the heat capacity of the heat-sensing material C:

$$\Delta T = \frac{E}{C}. \tag{8.119}$$

Since the heat capacity scales as the cube of the temperature T^3, best sensitivities are achieved by cooling calorimeter materials at cryogenic temperatures.

Bolometric devices are used in measurements of cosmic microwaves and in searches of dark matter.

Basic Calorimeter Signal Characterization

Hadronic and electromagnetic shower developments are stochastic processes. This implies that the signals produced by calorimeters exhibit relatively large fluctuations. The relative energy resolution of a calorimeter, $\delta E/E$, is thus an intricate function of the material used in its construction, its geometry, as well as the readout process. It is commonly described in terms of the empirical formula

$$\frac{\delta E}{E} = a \oplus \frac{b}{\sqrt{E}} \oplus \frac{c}{E}, \tag{8.120}$$

where the constants a, b, and c are determined by physical characteristics of the calorimeter, including the type of materials used and geometry, the technique used to generate and read out a signal, the amplification of the signal, and so on. The term a arises from nonuniformities in the construction and response of different modules, nonlinearities, while the term inversely proportional to $\sqrt{E}$ originates from the stochastic nature of the shower process. Roughly speaking, this stems from the fact that the shower contains a number of particle n proportional to the energy of the particle that initiated it. Each particle deposits a small amount of energy with some variance. The variance of the energy of the whole shower thus decreases with $\sqrt{n}$ and is inversely proportional to $\sqrt{E}$. The third component results mainly from instrumental effects that are energy independent (e.g., electronic noise). Its relative contribution thus decreases inversely with the energy.

Electromagnetic and hadronic showers have very different responses and resolutions. The resolution of electromagnetic showers is intrinsically limited by the variance of the path length of charged particles within the shower. For homogeneous calorimeters, it has been shown to be

$$\frac{\delta E}{E} \propto \frac{0.005}{\sqrt{E\ [\mathrm{GeV}]}}. \tag{8.121}$$

Fluctuations are quite a bit larger in sampling calorimeters, and one typically gets

$$\frac{\delta E}{E} \propto 0.04\sqrt{\frac{1000E_0}{E\,[\mathrm{GeV}]}}, \tag{8.122}$$

where E_0 represents the energy loss of a single charged particle in one sampling layer. Energy resolutions below the percent level are routinely achieved with homogeneous devices, but percent resolution appears to be a lower limit for E&M sampling calorimeters [81].

The resolution of hadronic shower calorimeters is larger still owing to fluctuations in the fractional energy loss of shower particles. Hadronic showers involve several processes, some of which produce muons, electrons, positrons, and slow neutrons. Because these particles have very different rates of energy deposition in the material, there are considerable fluctuations in the development and energy deposition of hadronic showers with resolution of the order of

$$\frac{\delta E}{E} \propto \frac{0.25 - 0.45}{\sqrt{E\,[\mathrm{GeV}]}}, \tag{8.123}$$

where the lower limit is achieved with perfect compensation for nuclear effects.

Hadronic showers tend to be spatially large, both transversely and longitudinally. The aforementioned performance is in fact possible only when the showers are fully contained within the active calorimeter volume.

Calorimeters are an essential component of high-energy physics detectors and have thus been the subject of considerable developments and performance studies [81, 194].

8.3.3 Measurements of Hit Positions

Measurements of particle hit position are an essential component of measurements of track momenta in magnetic spectrometers and particle detection with calorimeters. Hit position detectors are extremely varied in design, construction, and operation. At a basic level, the determination of positions relies on particle energy deposition in energy-sensing detector modules and components.

Charged Particle Energy Loss in Materials

Charged particles passing through matter interact with individual electrons and nuclei as well as the medium as a whole under appropriate conditions, leading to scattering, energy loss, Cherenkov radiation, and coherent bremsstrahlung. Scattering and energy loss dominate at intermediate energies: light projectiles (e.g., electrons) colliding with heavier target particles (e.g., nuclei) randomly deflect but lose relatively little energy unless they undergo inelastic collisions, whereas heavy projectiles colliding with lighter targets lose energy without being appreciably deflected. Repeated stochastic deflections of particles traversing a medium are predominantly caused by Multiple Coulomb Scattering (MCS). MCS degrades a spectrometer's capacity to determine the direction of a particle and thus introduces uncertainties in the determination of both the magnitude and direction of its momentum vector. Energy losses and fluctuations in energy loss degrade and smear the

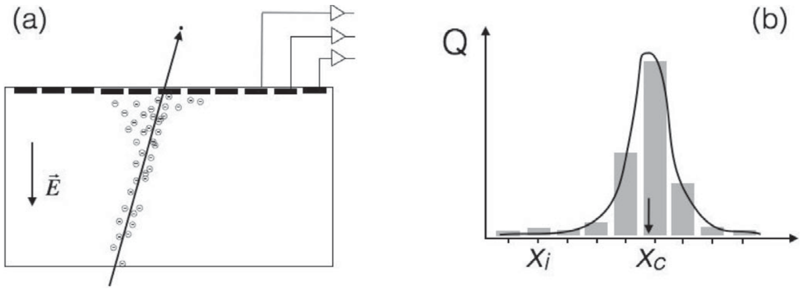

Fig. 8.20 Illustration of hit position determination based on charge sharing between contiguous energy deposition sensing components or cells.

momentum of particles and thus contribute to an additional loss of information and resolution. However, energy loss is a necessity in order to detect and analyze the trajectory of particles through detector layers, which enables tracking and momentum reconstruction. Additionally, because the energy loss of a particle depends on both its charge and momentum, measurements of energy deposition along a particle's trajectory make its identification possible (see §8.4).

Broadly speaking, position sensitive detectors can be grouped into two categories: those that sense the energy deposition but do not report its amplitude and those that do. This said, while hit sensing may be accomplished with either gas or solid state devices, basically all technologies rely on charge sharing between modules, illustrated in Figure 8.20, and discussed in the next section, to optimize the determination of hit position resolution.

A wide variety of hit-sensing technologies have been developed and are used in modern particle and nuclear physics experiments.

Characterization of the Performance of Hit-Sensing Detectors

Hit-sensing or position-sensitive devices that do not report the amount of energy deposited rely on a signal discriminator designed to "fire" and produce a logical pulse indicating the presence of a particle when the energy deposition in a cell (or module) exceeds a preset threshold. Detectors of this type do not require analog-to-digital converters (ADCs) and are thus considerably less expensive than more sophisticated devices that sense both the position and the amount of energy deposited. Their position resolution σ_x is, however, intrinsically limited by the width Δx of the sensing modules. Indeed, the variance of a uniform distribution (§3.4) across a finite width Δx determines the position resolution:

$$\sigma_x = (\mathrm{Var}[x])^{1/2} = \frac{\Delta x}{\sqrt{12}}. \tag{8.124}$$

The position resolution achievable with such devices is thus strictly limited by the granularity (width) of the modules.

Better performance can be achieved with devices of similar segmentation that also explicitly measure the energy deposition or charge collected. Improvement in the position resolution relies on energy or charge sharing between contiguous detector cells, illustrated schematically in Figure 8.20.

In gas and solid state detectors, energy deposition leads to the creation of electron–hole pairs. The number of electrons (or holes) produced may be sizable, ranging from several hundreds to tens of thousands. The charge diffuses and ends up spreading across several anode segments with an approximate Gaussian profile. Denoting the cell center positions as x_i and the energy or charge deposited in a given cell as w_i, an estimate of the hit position may be obtained from the distribution centroid

$$\bar{x} = \frac{\sum_i w_i x_i}{\sum_i w_i}, \tag{8.125}$$

where the sums are taken on contiguous cells forming a **cluster** of charge (or energy) deposition.

Considering a particle entering the segmented readout device at position x_0, let us assume the energy deposition and charge diffusion processes lead to a Gaussian distribution centered at the position x and with a width σ_x. Let Δx represent the width of the segments and x_i the center position. The expectation value of the charge N_i measured in segment i is thus given by

$$p_i = N \int_{x_i-\Delta x/2}^{x_i+\Delta x/2} e^{\frac{(x-x_0)^2}{2\sigma^2}} dx. \tag{8.126}$$

For a fixed number of electrons N, the diffusion process leads to charges $\vec{n} = (n_1, n_2, \ldots, n_m)$ on the m segments, forming a cluster with $\sum_i n_i = N$. The probability of observing $\vec{n}$ charges is given by a multinomial distribution $P(\vec{n}|N, \vec{p})$. The weights are $w_i = n_i$. The expectation value of the position $\bar{x}$ is thus

$$E[\bar{x}] = \frac{1}{N} \sum_i x_i E[n_i] = \frac{1}{N} \sum_i x_i p_i = x_0, \tag{8.127}$$

and its variance given by (see Problem 8.12)

$$\delta\bar{x}^2 \equiv \text{Var}[\bar{x}] = \frac{1}{N} \sum_i x_i^2 p_i - x_0^2 = \frac{1}{N} \sigma_x^2, \tag{8.128}$$

where $\sigma_x^2 = \sum_i x_i^2 p_i - x_0^2$ is the variance of the charge distribution. We thus conclude that the resolution of the charge cluster centroid is

$$\delta\bar{x} = \frac{\sigma_x}{\sqrt{N}}. \tag{8.129}$$

The segment width Δx should be chosen to be of order of the width σ_x. The centroid resolution thus improves in proportion to the square root of the number of electrons N. This implies that the resolution can be far better than $\Delta x/\sqrt{12}$ for large values of N. In practice, however, the presence of electronic noise limits the achievable precision, and the position resolution may be expressed as

$$\delta\bar{x} = a \oplus \frac{\sigma_x}{\sqrt{N}} = a \oplus \frac{b}{\sqrt{\langle E \rangle}}, \tag{8.130}$$

where $\langle E\rangle$ represents the typical energy deposition in a segment and a and b are two constants determined by the level of noise and the average ionization energy of the medium.

Time Projection Chambers (TPCs) achieve position resolutions of the order of 1 mm, while gas wire chambers routinely achieve position resolutions of the order of 200–1000 μm. Pixel and strip silicon detectors achieve even better resolution still with precision down to 5 μm.

8.4 Particle Identification

Although particle production models are constrained a great deal by measurements of inclusive (unidentified) particle production cross sections and correlation functions, studies of flavor dependencies of the particle production requires measurements of the cross section and correlation functions of precisely identified particle species (e.g., $\pi^{\pm}$, $K^{\pm}$, p, $\bar{p}$, etc.). While positively charged particles are readily distinguishable from negatively charged particles on the basis of the sign of their track curvature in a magnetic spectrometer, discriminating among particle species is a far more difficult task. Fortunately, several techniques and associated detector technologies have been developed over the years to achieve reliable Particle Identification (PID) on a particle-by-particle basis and enable specific measurements of particle-identified spectra and correlation functions.

In this section, we focus our discussion on PID techniques based on differential energy loss (§8.4.1) and time-of-flight (§8.4.2), whereas particle detection by invariant mass reconstruction of two- and three-body decays is presented in §8.5.1. Introductions to PID techniques based on Cherenkov radiation and transition radiation may be found in specialized texts [33, 21]. Discrimination of electrons against hadrons based on E&M calorimeter measurements is also possible [165].

8.4.1 PID by Specific Energy Loss

The energy loss of particles traversing thin media may be estimated with the Bethe–Bloch equation [35] for the specific energy loss dE/dx:

$$-\left\langle \frac{dE}{dx}\right\rangle = Kz^2\frac{Z}{A}\frac{1}{\beta^2}\left[\frac{1}{2}\ln\left(\frac{2m_ec^2\gamma^2\beta^2T_{\max}}{I^2}\right)-\beta^2-\frac{\delta}{2}\right], \tag{8.131}$$

where $K/A = 4\pi N_A r_e^2 m_e c^2/A = 0.307075\ \mathrm{MeV g^{-1} cm^2}$ for $A = 1\ \mathrm{g\,mol^{-1}}$; Z and A are the (average) atomic number and atomic mass of the absorber material; $N_A = 6.0221415\times 10^{23}\ \mathrm{mol^{-1}}$ is the Avogadro number; $m_ec^2 = 0.510998$ MeV is the mass of the electron ($\times c^2$); z is the charge (in units of the proton charge) of the incoming particle; β is the ratio of the speed of the incoming particle to the speed of light; $\gamma = (1-\beta^2)^{-1/2}$; I is the mean excitation of the absorber material (expressed in eV); and $\delta(\beta\gamma)$ is a density effect correction, which is typically small but becomes significant at very low and very

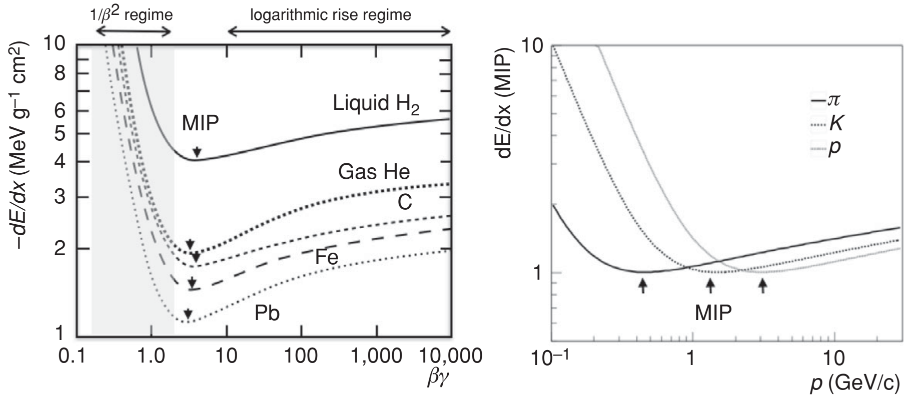

Fig. 8.21 (a) Specific energy loss of charged particles as a function of $\beta\gamma$ in selected materials. (b) Specific energy loss as function of particle momenta for pions, kaons, and protons. Arrows indicate minimum ionizing particle (MIP) values of $\beta\gamma$ and momentum. (Adapted with permission from J. Beringer et al. Review of particle physics. *Physical Review D*, 86:324–325, 2012.)

high momenta. The maximum energy $T_{\max}$ that can be transferred to an electron is given by [35]

$$T_{\max} = \frac{2m_e c^2 \beta^2 \gamma^2}{1 + 2\gamma m_e/M + (m_e/M)^2}, \tag{8.132}$$

where M is the mass of the incident particle. The mean excitation energy, I, is of the order of 10 ± 1 eV $\times Z$ for elements heavier than oxygen but it is recommended to use the well established values available in the scientific literature [35]. The specific energy loss predicted by the Bethe–Bloch equation is illustrated in Figure 8.21a as a function of $\beta\gamma$ for selected materials. It was verified experimentally that the formula provides estimates of the average energy losses that are accurate to within a few percents, for heavy particles with velocities in the range $0.1 \lesssim \beta\gamma \lesssim 1,000$ [35]. For values $\beta\gamma \lesssim 1$, the average energy loss is dominated by the first term of the Bethe–Bloch equation and thus features an approximate $1/\beta^2$ dependence on the particle's velocity. In this range, known at the $1/\beta^2$ energy loss regime, particles of different masses but equal speed have different momenta. It is thus possible to distinguish them on the basis of a plot of their energy loss vs. momentum, as illustrated in Figure 8.21b. The average energy loss reaches a minimum near $\beta\gamma \approx 3$, commonly referred to as the **minimum ionizing particle** (MIP). Distinguishing particles of same z but different masses in this range is, however, not possible based on their energy loss because they all feature essentially the same specific energy loss. For higher momenta, $\beta\gamma > 5$, the energy loss exhibits a slow rise with logarithmic dependence on $\beta\gamma$. Particle identification based on joint measurements of energy loss and momentum is thus possible in this **logarithmic rise regime**. The energy loss eventually saturates at very high momenta and the technique has therefore only a finite range of applicability.

Basic Principle

Identification by energy loss requires joint measurements of the momentum of a particle and energy loss through one or more energy loss sensitive devices. These two functions are often accomplished by distinct and dedicated detectors but can also be combined into a single device, such as a time projection chamber. The principle of the method is simple: measure the momentum and energy deposition of a particle in one or several detector layers, compute the average energy loss, and compare it to values expected for different species at the measured momentum. The species of the particle is that which most closely matches the measured average energy loss. This strategy works best in the low-momentum regime where the $1/\beta^2$ factor dominates the dependence of the energy loss and creates a large energy loss differential between particles of different masses. It also works in the logarithmic range regime. However, the technique is essentially ineffective for the MIP, that is, particles of intermediate momentum for which the $1/\beta^2$ saturates and the logarithmic term is not sufficiently large to enable a distinction of species.

Fluctuations and Straggling Functions

The identification of particle species based on their energy loss is complicated by two sources of noise commonly known as **process noise** and **measurement noise**. Process noise is associated with the physical process used to measure the physical observable at hand, whereas measurement noise refers to the noise present in the actual measurement, signal amplification, and readout. While the measurement noise can be minimized by careful design of the readout electronics, the particle energy loss and signal generation processes involve large event-by-event fluctuations that cannot be suppressed on an individual basis because they are largely determined by the physics of the collisions that engender energy losses.

Fluctuations in the energy deposition can be approximately modeled with the Landau distribution. Defining ξ as

$$\xi = 0.1535 \frac{z^2 Z}{A\beta^2} \rho(x), \tag{8.133}$$

the **Landau distribution** may be written

$$f_L(x, \xi) = \frac{\phi_L(\lambda)}{\xi}, \tag{8.134}$$

where

$$\phi_L(\lambda) = \frac{1}{2\pi j} \int_{r-j\infty}^{r+j\infty} \exp\left(u \ln(u) + \lambda u\right) du. \tag{8.135}$$

The variable r is an arbitrary constant and

$$\lambda = \frac{1}{\xi}\left(\Delta - \langle\Delta\rangle\right) - \beta^2 - \ln\left(\frac{\xi}{E_m}\right) - 1 + C_E, \tag{8.136}$$

with C_E the Euler constant. The function ϕ_L must be evaluated numerically, but is actually implemented in the ROOT package [59].

The Landau distributions shown in Figure 8.22a, calculated for three arbitrary values of mean and width, typify the large fluctuations in energy deposition that particles are subjected to as they pass through relatively thin detector layers. The large high side tail of the distribution, in particular, implies that the energy loss of low-mass particles (e.g., pions) may be mistakenly interpreted as being produced by heavier particles (e.g., kaons or protons). Since charged pion production typically dominates over kaon and proton production, the presence of a high side tail on the pion energy-loss distribution renders the identification of particles quite challenging, most particularly at the top of the $1/\beta^2$ range where energy-loss distributions produced by different pions, kaons, and protons considerably overlap.

The Landau distribution, derived from the Rutherford cross section, is suitable to illustrate the basic principle of particle identification by energy loss, but practical applications must account for a number of physical and instrumental effects. The energy lost ΔE by a particle in a detector volume is not necessarily entirely deposited within the sensing volume of the detector component. One must consider the conversion of the energy deposited D into ionization of the medium (whether gas or solid state). One must also consider the transport of electrons to the anode and the signal amplification of the proportional counter used to read out the signal. And finally, effects may arise in the digitization of the analog signal. Fluctuations in the energy loss and deposition have, however, been demonstrated to dominate the integrated charge Q measured in thin detector layers [39]. The measured distribution of energy Q are commonly referred to as **straggling functions** in the instrumentation literature. Bichsel has shown that finite corrections must be made to both the Bethe-Bloch formula and the Landau distribution to properly account for instrumental effects, particularly fluctuations in the energy deposition [39]. He published detailed parameterizations of the energy deposition and its fluctuations now commonly known as **Bichsel functions**. However, given the availability of computing functions for the calculation of Landau distribution (e.g., in ROOT), we illustrate the PID method based on the Bethe–Bloch and Landau distribution rather than the more complicated Bischel functions in the following sections.

Truncated Mean Technique

Particle identification may be accomplished based on a maximum-likelihood fit of the measured energy sample Q_i through the layers $i = 1, \ldots, m$ of energy-loss sensing devices. However, for the sake of simplicity, we here focus on a somewhat easier technique involving a truncated mean of the samples Q_i.

The standard deviation of the energy deposition in thin medium layers is typically rather large. However, by virtue of the central limit theorem (§2.10.4), the mean of a sample of m Q_i measurements should have a standard deviation of the order of $\sigma/\sqrt{m}$, where σ is the width of the parent distribution of energy loss of measured particles. Although the second moment of the Landau distribution is undefined (because the corresponding integral

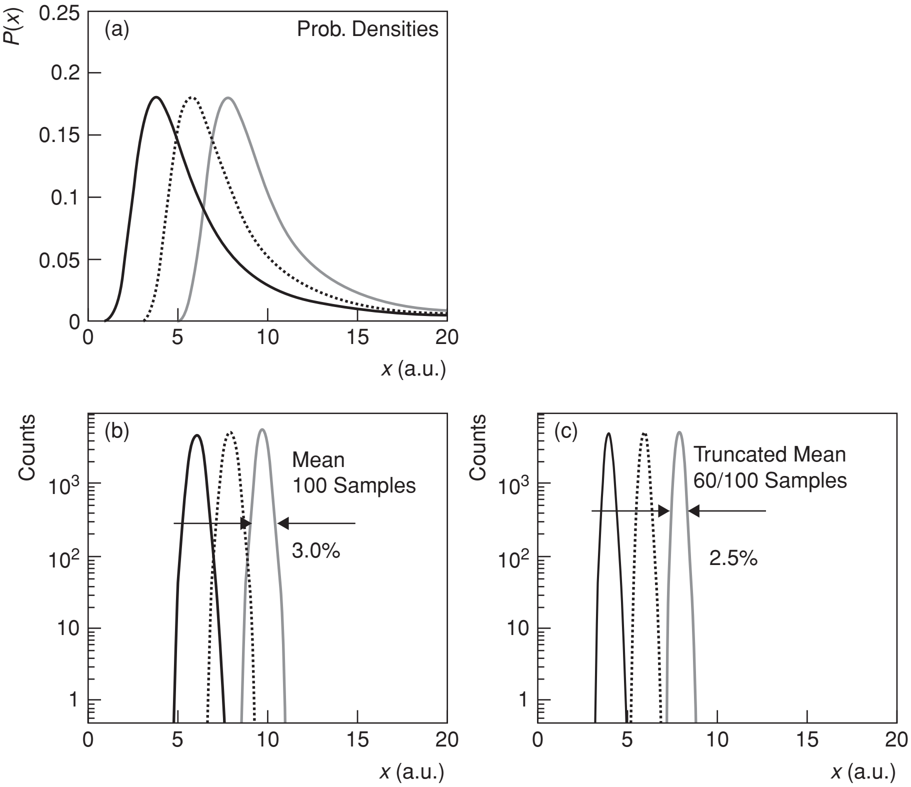

Fig. 8.22 Schematic illustration of the *dE*/*dx* truncated mean technique. (a) Probability densities of three particle species (with arbitrary means). (b) Distribution of the arithmetic means of 100,000 samples, each consisting of 100 values produced randomly with the distributions shown in (a). (c) Truncated mean distribution obtained with the 60 lowest values of each sample. Note that while the truncation introduces a bias on the value of the mean (i.e., a downward shift), it enables a sizable reduction of the dispersion of the mean which permits better separation of particle species shown in (c) relative to (b).

diverges), it is nonetheless possible to benefit from the $1/m$ reduction if a truncated mean of the sample values is used rather than the mean of the full sample. The principle of the truncated mean technique is simply to reject a suitably well chosen fraction f of the sampled values with the largest measured energy-loss values. Algorithmically, this is easily achieved by first sorting the n values of a sample of energy-loss measurements. One can then identify and eliminate the $f \times n$ largest values and calculate the arithmetic mean of the remaining values.

The rejection of the $f \times n$ largest values effectively truncates the high side tail of the Landau distribution, thereby producing a truncated average that features a nearly Gaussian distribution, as illustrated in Figure 8.22. The reduced fluctuations then yield dE/dx vs. p distributions that may provide good discrimination of species up to but excluding the MIP regime. The optimal fraction f is that which yields a truncated mean with the smallest standard deviation.

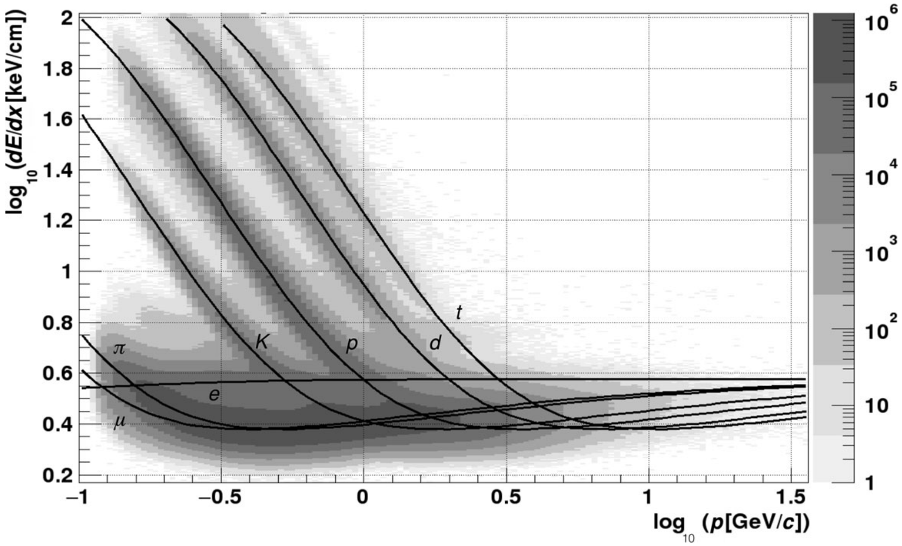

Fig. 8.23 *dE*/*dx* vs. *p* plot measured with the STAR Time Projection Chamber. One can readily distinguish bands corresponding to electrons, muons, charged pions and kaons, protons and antiprotons, deuterons and tritons. (Courtesy of Y. Fisyak and Z. Xu from the STAR Collaboration [83].)

The truncated mean technique is used in conjunction with several modern detectors. It is particularly useful for energy-loss measurements in gas detectors, such as time projection chambers, because fluctuations in energy deposition in such detectors can be rather large. As an example, Figure 8.23 displays an energy loss vs. p plot obtained with the STAR TPC, which exhibits excellent particle identification at low momenta [83].

Some Technical Considerations

It should be noted that the energy loss is a function of $\beta\gamma$: the measured truncated mean $\langle Q\rangle$ should thus be plotted as function of the momentum, not the transverse momentum. It is also important to account for the track geometry. The crossing angle of the track relative to the energy deposition sensing detector layer must be accounted for to properly calculate the energy loss per unit length within the sensing volume. For low-momentum tracks, it may also be necessary to account for the finite track curvature which may effectively increase the path length of a charged particle ΔL through the sensing volume, as illustrated in Figure 8.24.

8.4.2 Identification by Time-of-Flight

Basic Principle

The momentum of a particle is determined by its mass and velocity:

$$p = \gamma m \beta c, \tag{8.137}$$

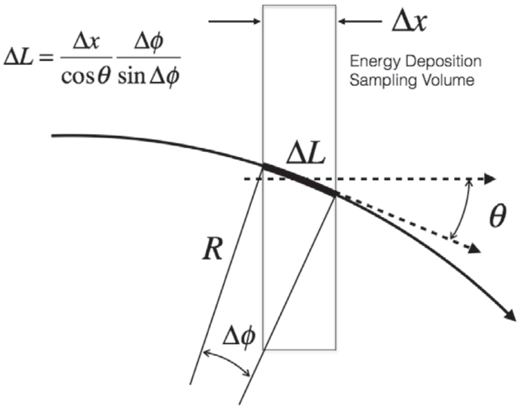

Fig. 8.24 For purposes of particle identification based on energy loss, the energy deposition measured in a detector volume must be scaled to account for the actual path length ΔL through the sensing volume of thickness Δx. The angle θ denotes the angle between the track direction and a normal to the detector plane. It may as such involve a component outside the bending plane. R and $\Delta\varphi$ represent the radius of the track and the angle subtended by the width of the module being traversed as measured from the center of the circular trajectory followed by the charged particle.

with $\beta = v/c$ and $\gamma = (1-\beta^2)^{-1/2}$. One can then use simultaneous or joint measurements of the momentum and speed of a particle to obtain its mass:

$$m = \frac{p}{\beta\gamma c}. \tag{8.138}$$

Such simultaneous measurements could be used to determine the mass of "new" particles (e.g., search for ultra-heavy nuclei), but in modern particle physics experiments they mostly serve to identify particle species, that is, to determine whether a given particle is a pion, a kaon, a proton, and so on. We here focus on such measurements designed to identify the species of observed charged particles in a magnetic spectrometer.

The momentum (or transverse momentum) is readily obtained from the radius of curvature of the charged particle in the bend plane. One must also obtain a measurement of the particle's speed. The most straightforward technique to determine the speed of a particle relies on a time-of-flight (TOF) measurement along a well-determined trajectory or flight path d. The trajectory is obtained from tracking, while a TOF measurement requires at least two timing detectors: one providing a start time t_{start} and the second a stop t_{stop}. The TOF of the particle, Δt, is thus nominally given by the difference of the times

$$\Delta t = t_{\text{stop}} - t_{\text{start}}, \tag{8.139}$$

and the speed is estimated according to

$$\beta = \frac{d}{c\Delta t}. \tag{8.140}$$

In principle, one can then use Eq. (8.138) to determine the mass of particles. In practice, various instrumental effects limit the precision to which Δt may be determined and β may then exceed unity. It is then preferable to calculate the square of the mass of the particle according to

$$m^2 = p^2 \left(\frac{1}{\beta^2} - 1 \right). \tag{8.141}$$

Obviously, the technique assumes that negligible energy/momentum losses occur along the particle's flight path and thus that the particle's momentum and speed remain constant throughout the measurement. In practice, corrections may be required to account for such effects.

TOF Measurements

In fixed-target experiments based on a magnetic dipole spectrometer, TOF measurements can be readily accomplished with two or more **TOF hodoscopes** as schematically illustrated in Figure 8.25a. In collider experiments, the need to reduce the thickness of materials along the path of measured particles and cost considerations typically dictate a design based on a single barrel-shaped array of TOF counters providing stop times and some form of interaction counter providing a **common start** for all TOF measurements, as schematically shown in Figure 8.25b. The flight path d relevant for the speed measurement is determined based on the geometry of the particles' trajectory. If two or more TOF hodoscopes are used, the relevant distance could be the flight path between the start and stop counters. In a collider geometry, one would typically use the trajectory from the collision primary vertex and the TOF counter. This requires that the start time, which is derived from interaction counters, be adjusted for the vertex position.

TOF measurements are based on the time of passage of a charged particle through timing detectors. In high-energy experiments, particles of interest have large momenta and thus speeds amounting to significant fractions of or even very close to the speed of light. The speed of light amounts to (approximately) 3×10^8 m/s. That corresponds to 30 cm per nanosecond. Given that typical detectors have sizes ranging from a few meters to several tens of meters, TOFs are rather short, ranging from several to tens of nanoseconds. Fast and highly accurate timing sensors are thus required. Diverse technologies may be used to conduct fast timing measurements, including fast scintillator detectors read out with **photomultipliers** (PMTs) or fast **avalanche photodiodes** (APDs), as well as multigap resistive plate chambers (MRPCs). The choice of technology is driven by cost and practicality. We here focus on the concept rather than the technical details of such measurements.

The principle of scintillator and MRPC counters is illustrated in Figures 8.26 and 8.27. Charged particles passing through a thin slab of scintillator material produce molecular excitations, which result in rapid photon emission. For an appropriately chosen material thickness, the number of emitted photons can be rather large and thus usable to establish a fast timing pulse. Well-designed scintillation counters feature geometry enabling fast light collection with high photon yield, minimal timing dispersion, coupled with fast and high-precision light sensors. The leading edge of the signal may then be used to produce a logic signal corresponding to the time of passage of the particle through the detector, as illustrated in Figures 8.26 and 8.27. Similarly, charged particles traversing an MRPC produce

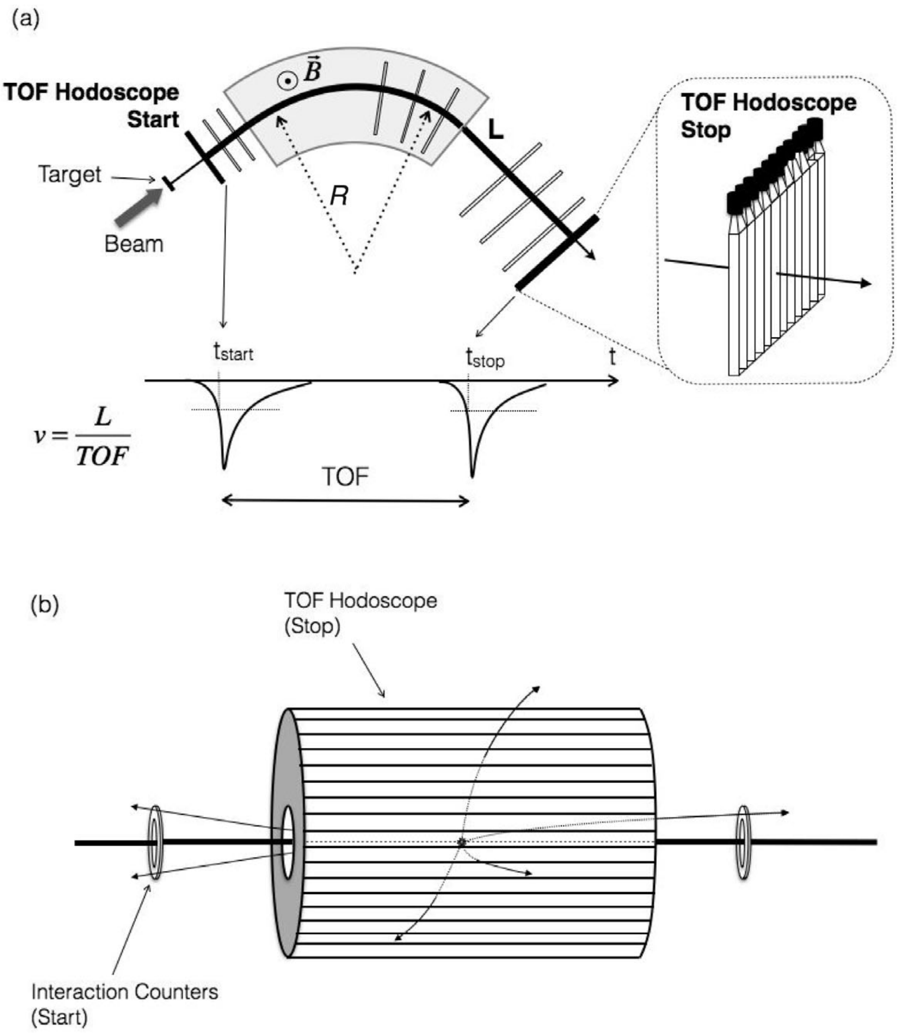

Fig. 8.25 Particle TOF hodoscopes in (a) fixed-target and (b) collider geometries may consist of sets of contiguous TOF scintillator modules read out by one or two light sensors (e.g., PMT, or APD). Alternatively, they may be based on multigap resistive plate chambers (MRPC). In collider geometry, interaction counters are commonly used to provide a TOF start, while barrel hodoscope counters provide a TOF stop, as schematically shown.

ionization within the gaps separating glass plates. The high voltage across gaps produces fast charge avalanches read out as image charge on segmented anodes. Low noise amplification of these signals produces fast rise time, which can also be utilized to produce logic signals fed into a time-to-digital converter (TDC) to obtain an actual timing measurement. A detailed discussion of TDC designs and technologies is beyond the scope of this text but may be found in several publications [99, 195].

TOF hodoscopes used in large particle and nuclear physics experiments typically involve from hundreds to thousands of distinct counters read out by fast electronics. They are

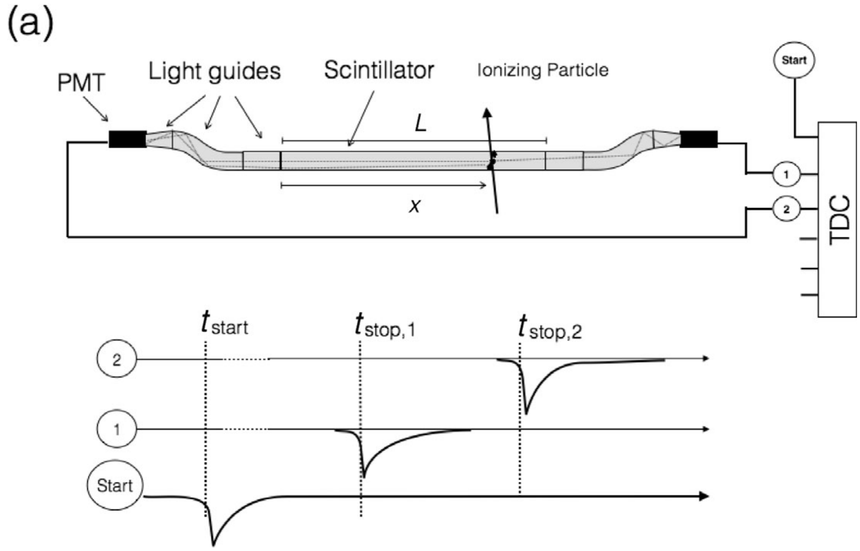

Fig. 8.26 Schematic illustration of the design of dual readout TOF scintillator counter modules.

usually equipped with TDCs featuring a digitization resolution of 25 ps and achieve TOF resolutions in the 50–100 ps range.

Practical Considerations

Signal collection, amplification, and transmission through cables and electronic components add an arbitrary but nominally fixed delay to the logic signals used to start and stop a TDC. In fact, delay cables often need to be added to electronics to produce start and stop logic signal inputs that fall within the counting range of TDCs. Changes in environmental conditions may, however, induce variations in signal propagation speed and must thus be accounted for in practice. The digitized times produced by TDCs then need to be calibrated to compensate for arbitrary and slowly varying offsets. This procedure, commonly known as t_0 calibration, is usually carried out based on a well-established reference, consisting either of identified particles at a precisely known momentum, or very high momentum particles that can effectively be assumed to travel at the speed of light. This calibration process must usually be carried out for each TOF counter individually and thus requires a fair amount of events. Also note that the calibration must be achieved with charged particle tracks acquired under normal running conditions (i.e., with the nominal magnetic field and trigger conditions).

Once the offsets are properly calibrated, the raw TOF is then obtained according to

$$\Delta t = t_{\text{stop}} - t_{\text{start}} + t_0. \tag{8.142}$$

Depending on the detector geometry and the type of readout, a number of additional corrections and calibrations may be required.

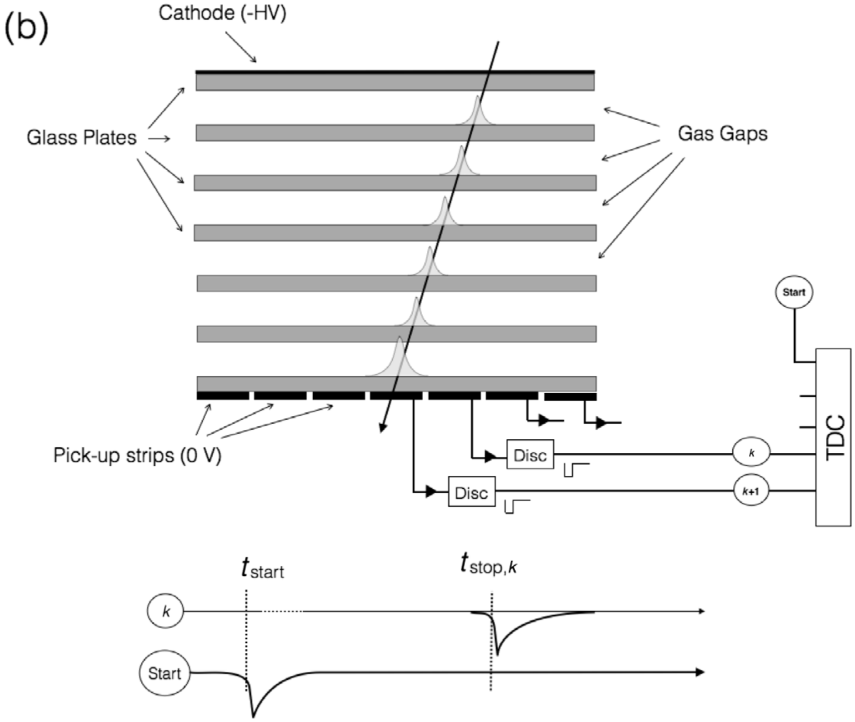

Fig. 8.27 Schematic illustration of the design of multigap resistive plate chambers (MRPCs).

In modern detectors, the generation of logic signals used by TDCs for TOF determination is achieved with **leading edge** discriminators whose principle of operation is illustrated in Figure 8.28. Leading edge discriminators use a voltage comparator with a fixed voltage threshold. The logic signals they produce thus exhibit a dependence on the amplitude of the incoming analog signal, known as "slewing": high-amplitude signals fire the discriminator early, whereas small-amplitude signals result in a later signal. Fluctuations in the energy deposition, charge (MRPC), or light (scintillators) production and collection result into timing fluctuations known as "jitter." While the slewing associated with pulse height dependence of the timing signal can be compensated by applying a correction based on the amplitude or leading edge slope of the signal, signal jitter is an intrinsic component of the signal and thus cannot be corrected for. Properly calibrated MRPC signals enable TOF resolution in the 50–100 ps range whereas scintillator counters achieve TOF resolution in the 70–100 ps range.

Particle Identification with TOF

Particle identification based on TOF and momentum measurements may be achieved by direct calculation of m^2 according to Eq. (8.141) or with selection criteria in the $1/\beta$ vs. p plane.

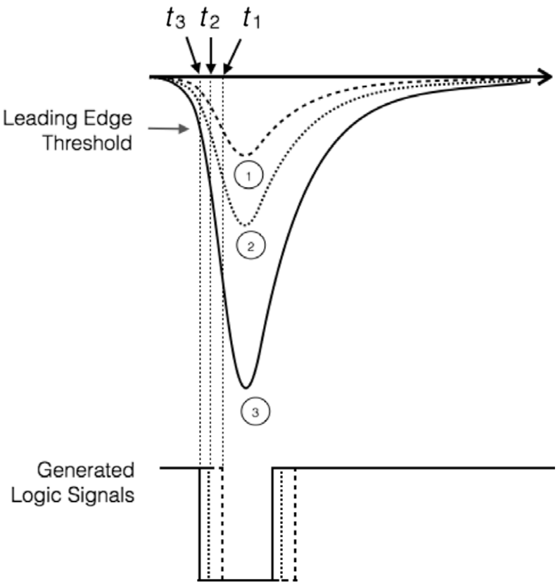

Fig. 8.28 Principle of leading edge discriminators used in the generation of timing signals in TOF measurements. A comparator issues a fast logic pulse when the input signal crosses a preset threshold. The use of a fixed threshold produces a delay, known as slewing, which depends on the signal amplitude. This undesirable effect is easily calibrated based on the signal amplitude and removed, in software, during the data analysis.

At a basic level, if the time-zero calibrations and corrections for hit position, light attenuation in scintillator counters, and amplitude dependence (slewing) are properly accounted for, Eq. (8.141) can be used to estimate m^2 and identify particle species. Evidently, the main technical challenge of such measurements is that high-momentum particles have high speeds whose accurate determination is largely determined by the TOF resolution and, to a lesser extent, by the momentum and path length resolution.

The mass resolution σ_m is simultaneously determined by the momentum resolution, σ_p, and the speed resolution, σ_β, which in turn depends on the TOF and path length resolution:

$$\sigma_m^2 \equiv \delta m^2 = \left(\frac{\partial m}{\partial p}\right)^2 \sigma_p^2 + \left(\frac{\partial m}{\partial \beta}\right)^2 \sigma_\beta^2 + \left(\frac{\partial m}{\partial p}\frac{\partial m}{\partial \beta}\right) \text{Cov}[p,\beta], \qquad (8.143)$$

where σ_p, σ_β, and Cov$[p,\beta]$ are the momentum resolution, the speed resolution, and the covariance between the momentum and the speed, respectively. Using Eq. (8.138), one finds

$$\frac{\sigma_m^2}{m^2} = \left(\frac{\sigma_p}{p}\right)^2 + \gamma^4\left(\frac{\sigma_\beta}{\beta}\right)^2 + \gamma^2\left(\frac{\text{Cov}[p,\beta]}{p\beta}\right). \qquad (8.144)$$

Note that Cov$[p,\beta]$ may be nonzero owing to the fact that the path length d, used in the calculation of β, depends on the momentum p. Such correlations are small, however, because the relative path length resolution is typically below 1%. The speed resolution is

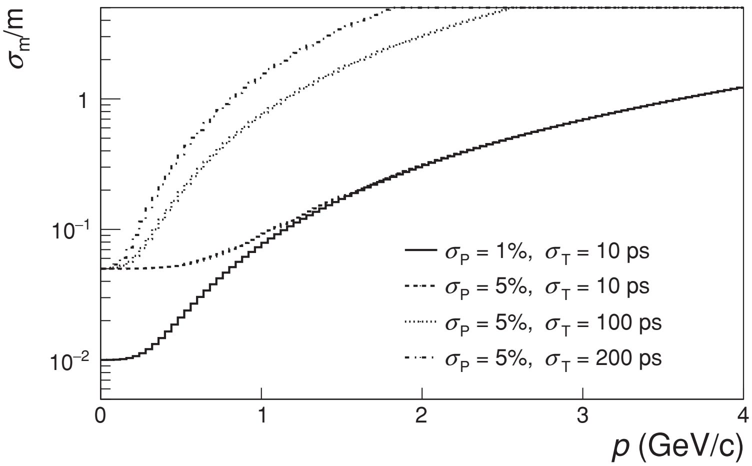

Fig. 8.29 Pion mass resolution obtained by TOF measurements as a function of momentum for selected resolution figures.

determined by the path length resolution and the TOF resolution

$$\frac{\sigma_\beta^2}{\beta^2} = \frac{\sigma_d^2}{d^2} + \frac{\sigma_T^2}{\Delta t^2}. \tag{8.145}$$

Overall, one finds, as illustrated in Figure 8.29, that the mass resolution is dominated by the momentum resolution for small values of β and $\gamma \approx 1$ and overwhelmingly driven by the (TOF) resolution for $\beta \approx 1$ and $\gamma \gg 1$.

Figure 8.30 displays the PDF of the mass of charged pions, kaons, and protons in the momentum range from 0.2 to 4 GeV/c for a flight path of 2 meters and selected momentum

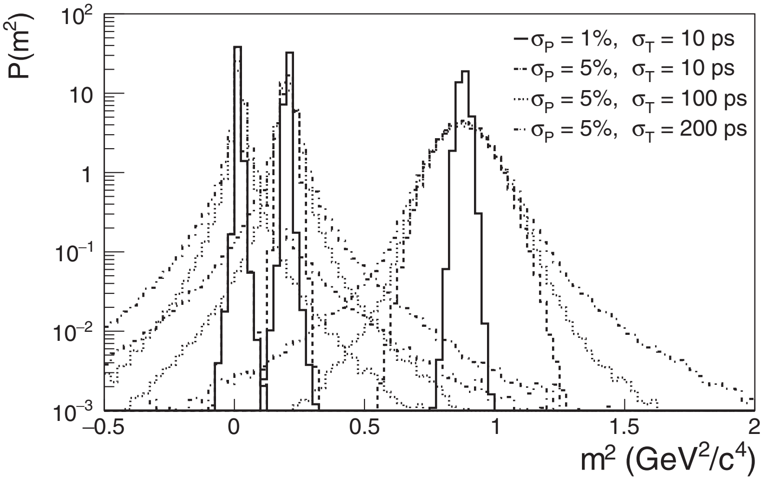

Fig. 8.30 Simulation of mass spectra obtained by joint measurements of momentum and TOF based on resolution figures shown for a 2-meter flight path.

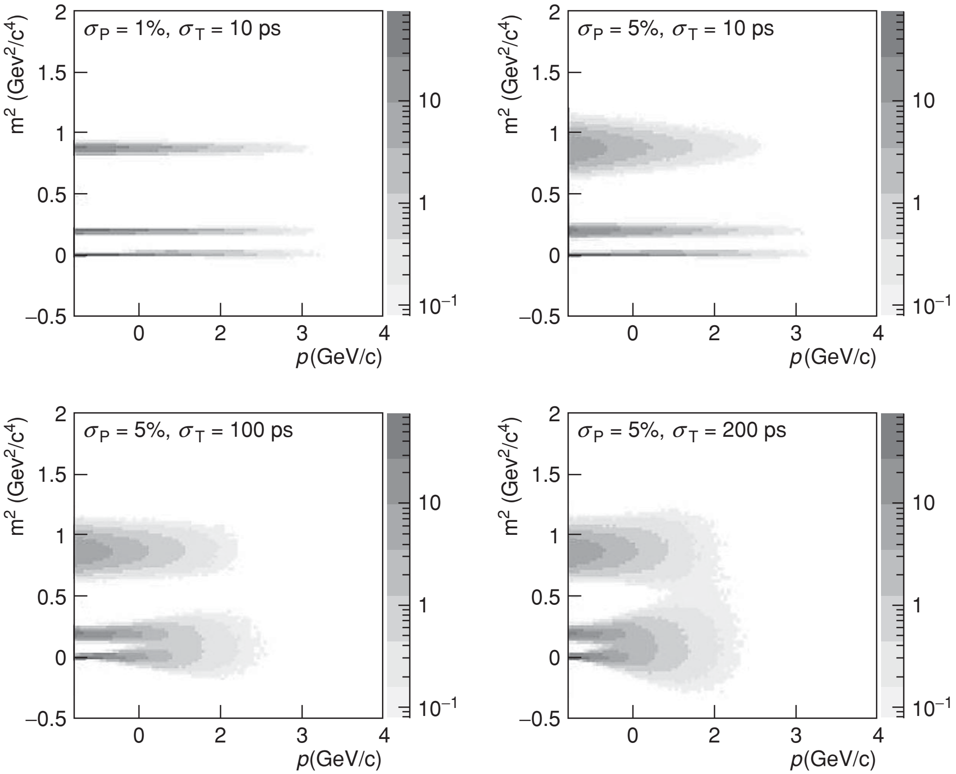

Fig. 8.31 Simulation of mass spectra vs. p obtained by joint measurements of momentum and TOF based on resolution figures shown.

and TOF resolution figures. The PDFs were generated by Monte Carlo simulations of the mass reconstruction assuming exponential spectra in momentum, with an average momentum of 0.5 GeV/c. The non-Gaussian profiles of the mass distribution stem from the momentum dependence of the mass resolution, as illustrated in Figure 8.31, which shows PDFs of the mass distribution as a function of the particle's momenta. One observes that at low momenta the mass resolution is indeed largely dominated by the momentum resolution, whereas at high momenta the saturation of speeds toward c implies that the finite TOF resolution leads to a significant broadening of the mass distributions.

Various biases in the determination of the particle's TOF may worsen the mass resolution embodied by Eqs. (8.143) and (8.145). It is then useful to plot the inverse of the measured speed, $1/\beta$, as a function of the momentum. In such a plot, particles of different mass populate different bands, as illustrated in Figure 8.32. It is thus possible to identify particle species on the basis of selection criteria in the $1/\beta$ vs. p plane. Losses of particles associated with these selection criteria or based on the reconstructed mass, Eq. (8.138), may be determined on the basis of realistic simulations of the detector response (see §14.2), as well as analyses of matched reconstructed tracks in the TOF counters.

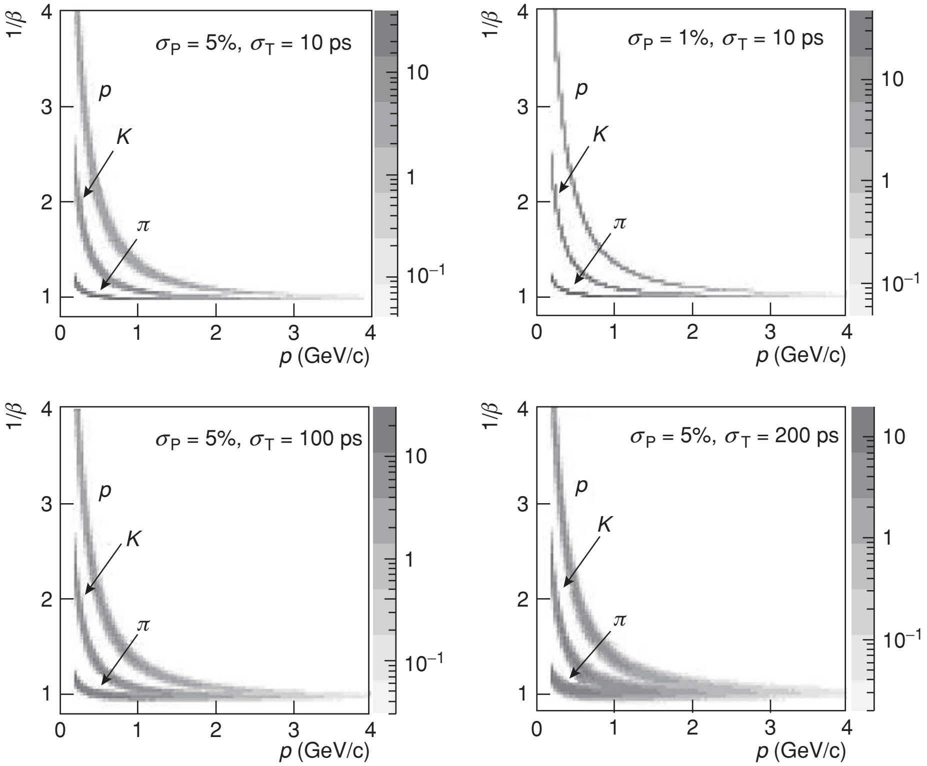

Fig. 8.32 PID based on plots of $1/\beta$ vs. p for selected momentum and TOF resolution figures.

8.4.3 Statistical PID and Semiexclusive Cross Sections

In studies of semiexclusive or species dependent cross sections, it seems natural to first utilize the information provided by energy-loss or TOF detectors to identify the species of particles, and subsequently proceed to increment relevant histograms as a function of the transverse momentum, rapidity, or azimuthal angle. One would then, in principle, obtain differential particle production cross sections that are specific to each particle type of interest (e.g., pions, kaons, protons, and so on). The problem arises, however, that unambiguous identification of particle species, particle-by-particle, is not always possible. As we saw in previous sections, unambiguous PID is difficult or impossible via dE/dx for particle momenta in the minimum ionization range or via TOF for particles with velocities $v \to c$. Measurements of semiexclusive (species dependent) cross sections as a function of transverse momentum (as well as rapidity and azimuthal angle) are nonetheless possible provided the dE/dx (or TOF) profiles of distinct species are sufficiently different and well known. Assuming, indeed, that the energy loss ΔE profile of each species k is known and can be described with a PDF $f_k(\Delta E|p)$, which is specific to each particle species being measured at a particular momentum p, one can then describe the inclusive energy loss profile according to

$$f(\Delta E|p) = \sum_{k=1}^{m} \mu_k(p) f_k(\Delta E|p), \tag{8.146}$$

where the parameters μ_k correspond to the relative contributions (or yield) of species $k = 1, \ldots, m$ of interest at the momentum p. So, rather than attempting identification on a particle-by-particle basis, it becomes possible to obtain cross sections by measuring a histogram of the energy loss as a function of the particle momenta. One then use the extended maximum likelihood method (§5.1.7) to carry out a fit to determine the coefficients μ_k, for each species, as a function of momentum (and other kinematic variables of interest). The coefficients $\mu_k(p)$ then effectively provide a measurement of the production yield of each of the species as a function of p or other kinematical variables of interest.

The technique is most straightforwardly applied to measurements of single particle cross section but can be extended to measurements of two- or multiparticle cross sections also.

8.5 Detection of Short-Lived Particles

While many particles produced in nuclear collisions are sufficiently long-lived to be measurable, for instance with a magnetic spectrometer, many particle species decay too rapidly to be observed directly. Their existence as collision products can nonetheless be identified on the basis of their decay particles. Two basic strategies are available to achieve their identification, each of which are discussed at a conceptual level in some details in the subsections that follow. The first strategy, known as the **invariant mass reconstruction** technique, relies on energy-momentum conservation and utilizes the measured momenta of decay products to calculate the mass of the decaying or **parent particle**. The second strategy relies on the **decay topology** and the presence of a **displaced vertex**. It is usable when the decaying particle is sufficiently long-lived to travel a measurable distance from its production location (primary vertex) before it decays (secondary vertex). This method is known as the **displaced vertex** technique and alternatively as the **decay topology** technique.

8.5.1 Invariant Mass Reconstruction Technique

Consider the two-body decay process illustrated in Figure 8.33. The parent particle has an unknown four-momentum p_p, and the decay products have 4-momenta p_1 and p_2. Energy-momentum conservation dictates that the sum of the 4-momenta of the decay products equals the four-momentum of the parent particle:

$$p_p = p_1 + p_2 = (E_1 + E_2, \vec{p}_1 + \vec{p}_2). \tag{8.147}$$

The square of the 4-momentum p_p yields the square of the mass, m_p, of the parent particle. A measurement of the momenta of the decay products and calculation of the square

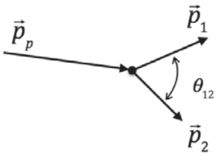

Fig. 8.33 Kinematics of two-body decays and invariant mass reconstruction.

of the sum of their 4-momenta thus enables identification of the parent particle species. If the PIDs of the decay products are known, one can indeed express these particles' energy in terms of the measured momenta and known masses:

$$E_i = \sqrt{|\vec{p}_i|^2 + m_i^2}. \tag{8.148}$$

However, if the PIDs are not known, one can formulate a specific hypothesis as to what their masses are and calculate energy estimates according to Eq. (8.148). The mass of the parent particle is thus given by the square of p_p:

$$\begin{aligned} m_p^2 &= E_1^2 + 2E_1E_2 + E_2^2 - |\vec{p}_1|^2 - |\vec{p}_2|^2 - 2\vec{p}_1 \cdot \vec{p}_2, \\ &= m_1^2 + m_2^2 + 2E_1E_2 - 2\vec{p}_1 \cdot \vec{p}_2, \end{aligned} \tag{8.149}$$

where in the second line we have used $m_i^2 = E_i^2 - |\vec{p}_i|^2$. Expressing the energies of the decay products in terms of their momenta, we get

$$m_p^2 = m_1^2 + m_2^2 + 2|\vec{p}_1||\vec{p}_2| \left(\sqrt{1 + \frac{m_1^2}{|\vec{p}_1|^2}} \sqrt{1 + \frac{m_2^2}{|\vec{p}_2|^2}} - \cos\theta_{12} \right),$$

where θ_{12} represents the angle between the momenta $\vec{p}_1$ and $\vec{p}_2$. For $|p_i| \gg m_i$, the preceding simplifies to

$$m_p^2 = m_1^2 + m_2^2 + 2|\vec{p}_1||\vec{p}_2| \left(1 - \cos\theta_{12}\right), \tag{8.150}$$

and the mass resolution is then typically limited by the momentum resolution, as illustrated in Figure 8.34, and to a lesser extent by the precision of the angle θ_{12}.

Combinatorial Background

In principle, the technique described in the previous section enables the identification of decaying particles of specific mass. In practice, nuclear collisions, particularly those of relativistic heavy ions, produce a large number of particles, and there is no way (other than the technique described in §8.5.3) to identify which particle pair was actually produced by a decaying particle.

Consider, for instance, an event consisting of n particles in which two (and only two) particles were produced by the decay of a short-lived particle. To find out which two particles might originate from the decay, one must examine all $n(n-1)/2$ particle pairs that can be formed by combining n particles, and calculate their invariant mass according to

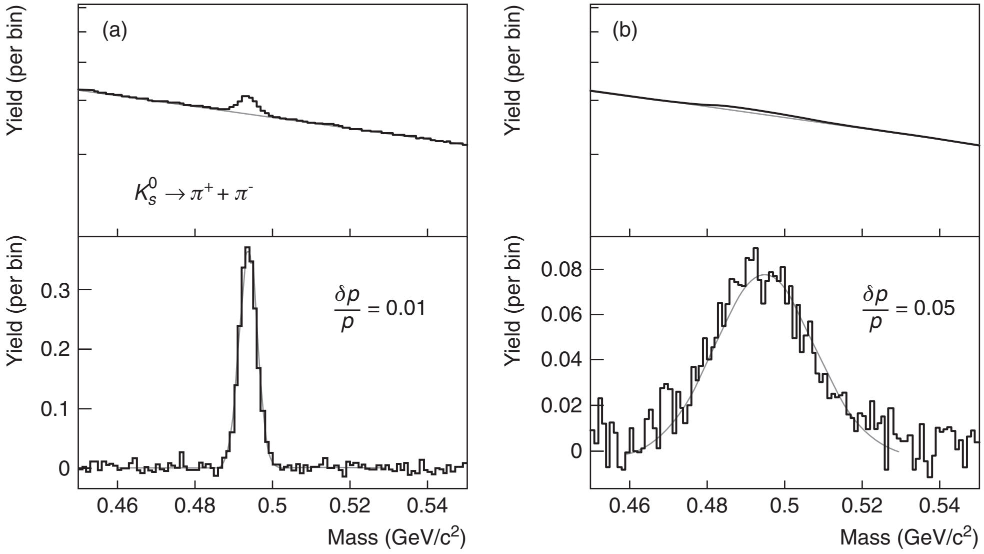

Fig. 8.34 (Top) Simulations of 100,000 "real events" (solid line) and "mixed events" (dotted lines) invariant mass distributions of $K_s^0 \to \pi^+ + \pi^-$ decays with finite momentum resolution, $\delta p/p = 0.01\%$ (left) and $\delta p/p = 0.05\%$ (right). Simulated events feature an average of two measurable kaons decays and 50 background pions per event. The mixed-event distribution is normalized to have equal yield per event as the real distribution at $m = 0.6$ GeV/c^2. (Bottom) net kaon mass spectrum determined from the subtraction of actual and mixed events distributions, where the solid line shows a Gaussian+constant background fit to the kaon mass spectrum.

Eq. (8.150). However, particles not produced by a decay have no specific relation: they can be separated by an arbitrary angle and have arbitrary momenta. Their invariant mass is not constrained and can then cover a very wide range of values. The $n(n-1)/2-1$ unrelated pairs thus constitute a **combinatorial background** to the one true correlated pair (by decay) that covers a wide range of masses, as illustrated in Figure 8.34. The shape and spread of the background are largely determined by the steepness of the single particle spectrum, the kinematical (p_T) range, and the angular range of the acceptance. They may also be influenced by resolution (smearing) effects associated with the reconstruction of the particles constituting the event. All in all, distinguishing one particular pair out of a group of $n(n-1)/2-1$ unrelated pairs consequently amounts to an impossible challenge if attempted for a single event. Fortunately, one is generally not interested in detecting a particular decaying particle but rather in measuring the production yield of such particles as a function of transverse momentum, production angle, and so on. It is then possible, at least in principle, to obtain a large sample of decays by examining a large number of distinct events. There remains the task of determining and subtracting the combinatorial background in order to determine the production cross section of the short-lived particles. We describe techniques to achieve this result in the next paragraph. We additionally describe a technique based on the decay topology, usable for decays with a displaced vertex, in §8.5.3.

Background Subtraction and Signal Determination

The determination of the decaying particle yield may be achieved by a variety of methods, including the bin summing method, the fit method, or the combinatorial background removal method, each discussed in the following.

Bin Summing Method

If the background can be properly subtracted (with either of the methods described in the text that follows), it may be sufficient to sum the yields observed in invariant mass bins surrounding the expected mass peak:

$$Y = \sum_{\text{peak}} y_i, \tag{8.151}$$

where y_i represent the yield in bins surrounding the mass peak after background subtraction. The statistical error, δY, on the integrated yield Y can then be estimated as the sum, in quadrature, of the errors in each bin included in the sum:

$$\delta Y = \sqrt{\sum_{\text{peak}} \delta y_i^2}. \tag{8.152}$$

Proper selection of the number of mass bins included in the sum is important and must reflect the actual (or expected) peak width, including smearing effects. On the one hand, if the number of bins included in the sum far exceeds the actual width of the signal peak, the yield may end up being biased by improper background subtraction and the yield uncertainty is likely to be overestimated. On the other hand, if the number of bins is too small, only a fraction of the signal can be integrated. This results in an efficiency loss that can be estimated, and thus corrected for, if the signal shape and its width can be properly estimated.

Fitting Method

The fitting method relies on a line fit of the signal and (combinatorial) background. In cases where the signal line shape is dominated by smearing effects, it is often possible to model the signal peak with a Gaussian distribution and the background with a polynomial, as illustrated in Figure 8.34:

$$f(m) = \sum_{n=0}^{n_{\max}} a_n m^n + \frac{Y}{\sqrt{2\pi}\sigma} \exp\left(-\frac{(m-m_o)^2}{2\sigma^2}\right), \tag{8.153}$$

where the coefficients a_n must be adjusted to fit the combinatorial background, while Y represents the yield of decaying particles, m_o is the centroid of the mass peak, and σ its width determined by the resolution of the mass measurement. If smearing effects are negligible, the peak line shape can generally be modeled with a Breit–Wigner distribution (Eq. 3.179), whereas if smearing effects are finite but not dominant, one must fold the Breit–Wigner line shape with the detector smearing function (typically a Gaussian):

$$f(m) = \sum_{n=0}^{n_{\max}} a_n m^n + \frac{Y}{\sqrt{2}\pi^{3/2}\sigma} \int e^{-\frac{(m-m')^2}{2\sigma^2}} \frac{\Gamma/2}{\Gamma^2/4 + (m' - m_o)^2} dm'. \qquad (8.154)$$

The line shape may optionally have to be adapted to various kinematical conditions.

Given that invariant mass spectra are usually obtained with finite bin width histograms, fits should be carried out using integrals of the preceding functions across the width of the mass bins. An option to accomplish fits with such integrals is conveniently provided in the ROOT fitting package [59]. There are cases where multiple peaks may be present, and one must then model them accordingly using multiple peak functions.

Combinatorial Background Removal:

When the number of combinatoric pairs, $n(n-1)$, is very large, a direct fit to the spectral line shape may become impractical. This is the case, in particular, when the background shape is complicated and cannot be readily modeled with a simple function (as earlier). It is then necessary to model the background based on the data itself. This can be accomplished, for instance, by producing mass spectra obtained from mixed events (§12.4.5). Particles from mixed events are uncorrelated by construction and should thus not produce a mass peak. However, they should provide a reasonable model of the combinatorial background. Since the shape of the combinatorial background may depend on the shape of the particle spectrum, kinematical selection criteria, and so on, it is important to carry out subtraction based on mixed events that have similar characteristics (e.g., multiplicity, kinematical, and quality selection criteria) as the actual events.

Additionally, since the multiplicity of real and mixed events may differ, so will the number of pairs that can be formed in real and mixed events. It is thus necessary to normalize the amplitude of the mixed events "combinatorial" background to match the amplitude of the real background. This can be typically accomplished by arbitrarily scaling the mixed-event mass spectrum such that its yield at a mass m_s several standard deviations away from the peak of interest equals the yield of the real pair spectrum at the same mass m_s. If the production of mixed events is not possible, another technique involves randomly rotating tracks in azimuth or reshuffling the particles in pseudorapidity (i.e., randomly setting the rapidities but keeping the same p_T values), or both.

It is important to note that the mixed- and real-event combinatorial background shapes may differ substantially. The background subtraction shall consequently be imperfect and constitutes a source of systematic error. One must then typically utilize a parameterization of the background to fit and remove the remaining background, as discussed earlier. Differences may occur owing to a variety of physical and instrumental effects, including correlations between particles which are present in the final state of collisions because of (broad) resonance decays, cluster or string decays, jets, or correlated backgrounds. The latter may be generated in the apparatus by correlated electron–positron pairs produced by photon conversion, and possibly also event-to-event variations in the acceptance or efficiency of the detection system. Such effects can in principle be studied with Monte Carlo simulations.

Statistical and Systematic Errors on Yields

The statistical uncertainty on yields obtained with the bin summing method is given by Eq. (8.152). Estimates of the error on the yield obtained with the fit method can in principle be obtained directly from the fit if the fit includes both the signal and the background. If the fit does not include the background, one must add the uncertainty on the yield ($\delta Y = \sqrt{Y}$) and the uncertainty on the background. The background uncertainty may involve a global uncertainty and bin-to-bin uncertainties.

Systematic errors involved in the determination of short-lived particle yields are diverse and may include both physical backgrounds and instrumental effects. Physical backgrounds include broad underlying resonances and invariant mass structures caused by particle correlations in the final state; instrumental effects include uncertainties in the evaluation of the particle reconstruction efficiencies and acceptance, invariant mass spectrum structures caused by resolution effects or discretization of the kinematical parameters used in the invariant mass reconstruction (particularly angles), and instrumental sources of background such as electron–positron production and generation of tertiary particles within the detection apparatus. In practice, many of these sources of uncertainties become linked or correlated within the context of the background subtraction, and it may not be appropriate to quote them as distinct and independent sources added in quadrature.

Systematic uncertainties associated with the background subtraction may be estimated by generating several distinct but equally plausible backgrounds and signal line shapes. The mean and variance of the resulting yields may then be used to estimate the signal strength and systematic uncertainties associated in its determination. For instance, if fits of the background with, say, three different models (e.g., first-, second-, or third-order polynomials) and three different ranges of mass yield similarly acceptable χ^2 values, it is legitimate to carry out a measurement of the yield above background with either of these models and ranges. One can then use the mean of the yields obtained in each of these cases as the estimate of the production yield and obtain a systematic error based on their standard deviation. If the yields obtained with the different backgrounds and fit models are Gaussian distributed and can be considered uncorrelated, then their standard deviation can be considered as one σ systematic error with a confidence level of 68%.

8.5.2 Three-Body Decays and the Dalitz Plot

A three-body decay involves the disintegration of a particle of mass M into three lighter particles of mass m_i, $i = 1, 2, 3$, as illustrated in Figure 8.35a. Unlike two-body decays where the momenta of the decay products are completely specified by energy-momentum conservation, three-body decays involve additional degrees of freedom. Different values of momenta are indeed possible depending on the decay configuration as shown in Figure 8.35b. Dalitz [74, 75] realized that the angular momentum of the parent particle largely

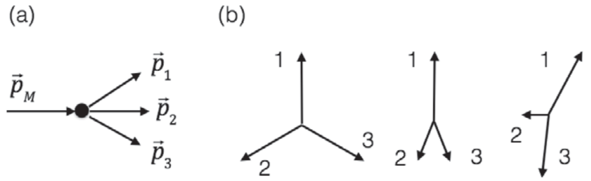

Fig. 8.35 (a) Kinematics and (b) topologies of three-body decays.

determines its decay configuration. Observations of the relative frequency of different configurations of decay products thus provides insight as to the spin of the decaying particle.

In a two-body decay, the four momenta of the decay products nominally amount to eight free parameters. However, energy-momentum conservation reduces this number to four, and the relations between energy and momentum, $E^2 = p^2 + m^2$, further reduces this number to only one free parameter, which can be taken as the invariant mass of the decay particles. In a three-body decay, there are three four momenta and thus twelve parameters. Momentum conservation reduces this number to eight, and the relation between energy-momentum further reduces the number to four parameters. In the rest frame of the parent particle, the three decay products are within a plane of arbitrary orientation. Given that it takes two angles to determine the orientation of this plane, the number of free parameters is further reduced to two units: a three-body decay has thus two degrees of freedom. Many options exist in the selection of two variables for the description of a three-body decay. Dalitz [74] originally used variables x and y, defined as

$$x = \sqrt{3}\frac{T_1 - T_2}{Q}, \tag{8.155}$$

$$y = \frac{2T_3 - T_1 - T_2}{Q}, \tag{8.156}$$

where T_i, $i = 1, 2, 3$ represent the kinetic energy of the three decay products and Q is the energy released by the decay:

$$Q = M - m_1 - m_2 - m_3. \tag{8.157}$$

However, it is now more common to analyze three-body decays in terms of the square of invariant masses m_{12} and m_{13}, defined as

$$m_{ij}^2 = p_{ij}^2 = \left(E_i + E_j\right)^2 - \left(\vec{p}_i + \vec{p}_j\right)^2. \tag{8.158}$$

One may then represent decays in a **Dalitz plot**, according to their position in the plane m_{23} and m_{12}, as schematically illustrated in Figure 8.36. In the rest frame of the parent particle, the invariant mass of a given pair, say m_{12}, has a minimum value $m_1 + m_2$ if particles 1 and 2 are produced at rest relative to each other, and it takes a maximum value $M - m_3$ if particle 3 is produced at rest relative to the parent. These and similar conditions for m_{23} define the boundaries shown as dashed lines in Figure 8.36. In between these extremes, a specific value of m_{12} limits the energy accessible to the pair 23 and thus defines minimal and maximal values shown by arrows in the figure.

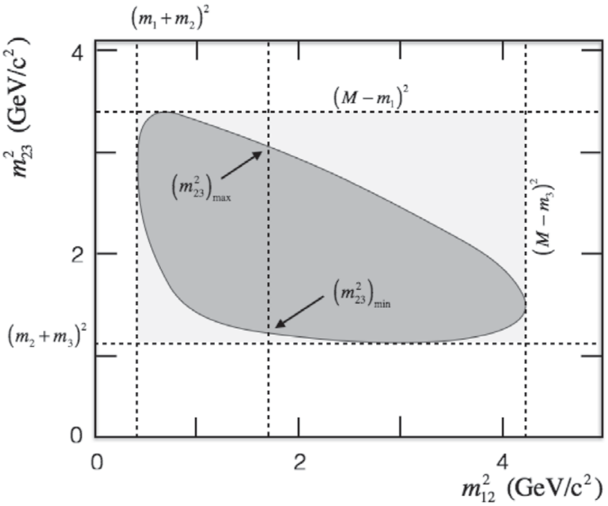

Fig. 8.36 Schematic illustration of a Dalitz plot used in the study of three-body decays. The dark gray area indicates kinematically allowed values while the dashed lines delimitating the light gray area define basic kinematic limits achieved when two daughter particles are emitted at rest relative to each other, or one produced at rest relative to the parent particle.

A Dalitz plot constitutes a **ternary plot**, that is, a plot involving three variables constrained by a condition. Choosing, for instance, m_{12}, m_{13}, and m_{23}, one readily finds (see Problem 8.9)

$$m_{12}^2 + m_{13}^2 + m_{23}^2 = M^2 + m_1^2 + m_2^2 + m_3^2. \tag{8.159}$$

One additionally finds

$$m_{12}^2 = (P - p_3)^2 = M^2 + m_3^2 - 2ME_3, \tag{8.160}$$

where E_3 is the energy of the third particle in the rest frame of the decaying particle.

In the absence of angular correlations (e.g., parent particle with $J = 0$), the distribution of the decay products in m_{12} vs. m_{13} is expected to be flat. However, symmetries may impose various restrictions on the distribution of decay products. Additionally, resonant decays in which the parent particle first decays into two particles, with one of the decay products readily decaying into two additional decay products, often dominate three-body decay processes and are manifested by the presence of peaks around the mass of the resonant decay, as shown in Figure 8.37. As such, the Dalitz plot provides a useful tool for investigating the dynamics of three-body decays. The technique can be adapted to four-body decays as well [171].

8.5.3 V^0 Topological Reconstruction Technique

Several "short-lived" elementary particles (e.g., K_s^0, Λ^0, Σ, Ds, and their antiparticles) have lifetimes sufficiently long to be observable based on their decay topology and displaced

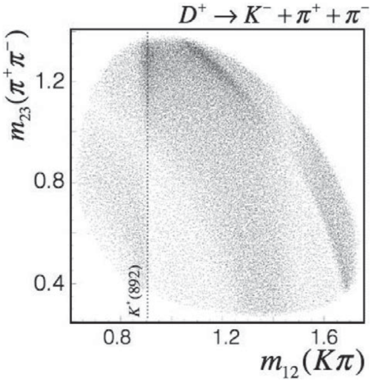

Fig. 8.37 Example of Dalitz plot for $D^{+-} \longrightarrow K^- + \pi^+ + \pi^+$ decays measured by the CLEO Collaboration in $e^+ + e^-$ collisions at $\sqrt{s} = 3.770$ GeV. The peaked structure of the plot along the m_{12} axis stems from the fact that D-mesons may decay into K^*, which subsequently decays into $K + \pi$. (Courtesy of G. Bonvicini from the CLEO Collaboration [51].)

vertex. Kaons (K_s^0), lambdas (Λ^0), cascades (Ξ^0), and omegas (Ω^-) were in fact discovered in bubble chamber experiments based on their decay topology. For instance, Figure 8.38 displays the first observed Ω decay, by Barnes et al. [27], with the BNL 80-inch hydrogen bubble chamber on the basis on its unique sequence of charged-track topologies. In general, decays of neutral particles produce V-shaped topologies of charged particle tracks and are, for this reason, commonly called V^0 **particles** or V^0 **decays**. The phrase "V^0 particle" is

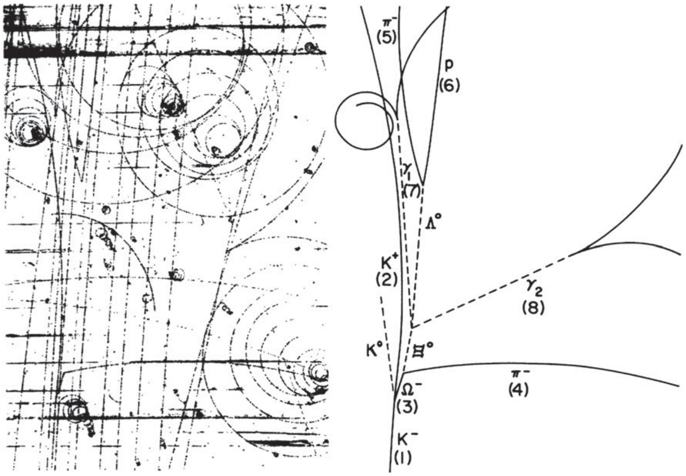

Fig. 8.38 (Left) Photograph of a bubble chamber event showing the first reported $^-$ decay [27]. (Right) Analyzed trajectories: solid lines represent observed charged particles while dashed lines indicate reconstructed trajectories of decayed neutral particles. The $^-$ decays into a π^- and a/^{0}, which subsequently decays into a $\|^0$ and two photons (γ_1 and γ_2). The $\|^0$ itself decays into a proton (p) and a π^-. (Reproduced with permission from V. E. Barnes, et al. Observation of a hyperon with strangeness minus three. *Physical Review Letters*, 12:204–206, 1964.)

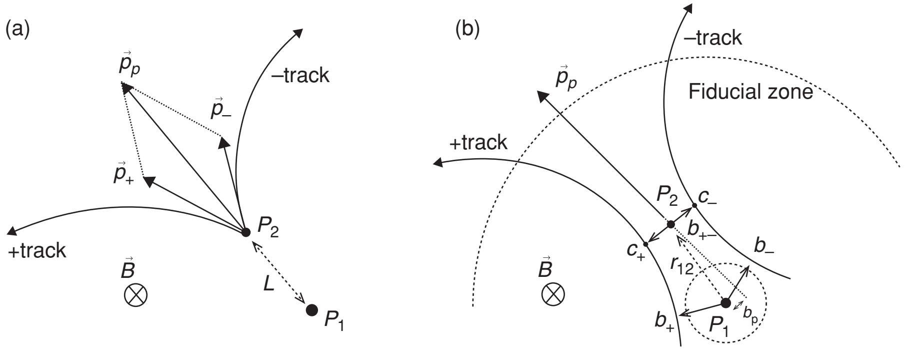

Fig. 8.39 (a) Nominal and (b) actual V^0 decay topologies in a uniform magnetic field with definitions of selection criterion variables typically used in V^0 analyses.

also often used as a generic term that includes all particles decaying with a measurable displaced vertex, whether neutral or not.

Principle of the V^0 Reconstruction Technique

The nominal spatial configuration of a V^0 four decay in a uniform magnetic field is illustrated in Figure 8.39 (a). A neutral particle of four-momentum p_P produced at the primary vertex P_1 propagates a certain distance L before it decays at the **secondary vertex** P_2 into a pair of charged particles with four-momenta p_+ and p_-. By virtue of energy-momentum conservation, one has $p_P = p_+ + p_-$, and Eq. (8.150) provides for an estimate of the mass $m_P = (p_P \cdot p_P)^{1/2}$ of the neutral particle. For sufficiently large values of L, such decay topologies are readily visualized in bubble chamber detectors or photo emulsions. They can also be reconstructed and identified with multilayered tracking detectors, as schematically illustrated in Figure 8.39b. However, finite position resolution and scattering effects smear the reconstruction of charged particle trajectories, and one consequently ends up with tracks that do not feature perfect decay topologies; that is, they do not intersect at the decay point P_2. In a very low track multiplicity environment, even imperfect track topologies such as the one schematically illustrated in Figure 8.39b may be readily identifiable as V^0. In practice, uncertainties arise due to finite decay lengths L, combinatorial effects associated with large track multiplicities, and limited track resolution. The identification of V^0 must then rely on extensive sets of topological and kinematical selection criteria designed to distinguish true displaced vertex decays from **combinatorial decays** (also called fake decays).

We discuss the definition and use of topological selection criterion in the next paragraph, and consider technical details of their calculations in the following paragraphs.

Topological and Kinematical Selection Criteria

V^0 reconstruction analyses typically involve all or a subset of selection criteria based on variables introduced in Figure 8.39b.

DCA b_{+-} of the Daughter Tracks

Tracks produced by a decay must originate from the secondary vertex P_2. The trajectories of these **daughter tracks** must then intersect or nearly intersect near P_2. The distance of closest approach (DCA) between the two tracks, b_{+-}, as defined in Figure 8.39b characterizes how closely any two tracks intersect. Ideally, this distance should be null for true daughter tracks. In practice, given smearing effects associated with track reconstruction resolution, b_{+-} is finite and characterized by a PDF $P_{\rm DCA}(b_{+-})$ of width σ_{+-} for actual daughter tracks; in contrast, combinatorial pairs of tracks feature a much wider, nearly uniform distribution of values. It is thus legitimate to use a selection criterion $b_{+-} \le b_{\max}$ to eliminate combinatorial track pairs. The nominal efficiency of the selection criterion is then

$$\varepsilon_{+-} = \int_0^{b_{\max}} P_{\rm DCA}(b_{+-})\, db_{+-}. \tag{8.161}$$

The level of contamination leaking through this selection criterion depends on the track reconstruction resolution, the proximity of the decay point P_2 to the primary vertex P_1, as well as the overall track multiplicity of the event. Other selection criteria are thus necessary.

Distance r_{12} between the Secondary and Primary Vertices

One estimates the position of the secondary vertex P_2 as the bisection of a segment joining points C_+ and C_- corresponding to the points of closest approach between two tracks. The variable r_{12} characterizes the distance between the estimated position of the secondary vertex and that of the primary vertex. Nominally, for true daughter pairs the distance r_{12} should exhibit an exponential distribution with a decay constant $\gamma c\tau$ determined by the lifetime τ and the speed distribution of the parent particle. For sufficiently large values of r_{12}, the number of combinatorial pairs is null or negligible, but for small values, primary particles may contribute a sizable background. It is thus useful to require that r_{12} exceeds a minimum value $r_{12,\min}$ determined largely by the DCA resolution of primary tracks. In practice, one may also use an upper limit $r_{12,\max}$. The values $r_{12,\min}$ and $r_{12,\max}$ thus define the fiducial volume of the measurement. Given that particles decay stochastically with an exponential distribution, these two criteria produce a loss of decaying particles with an efficiency of the order of

$$\varepsilon_r = \frac{1}{\lambda}\int_{r_{12,\min}}^{r_{12,\max}} \exp\left(-\frac{r_{12}}{\lambda}\right) dr_{12}, \tag{8.162}$$

where $\lambda = \bar{\gamma} c\tau$ corresponds to the effective decay length determined by the (average) speed and lifetime of the decaying particles.

DCA of the Parent Relative to the Main Vertex

The sum of the momentum vectors of the two daughter tracks nominally adds to the momentum of the parent particle, $\vec{P}$. The momentum vector $\vec{P}$ and the point P_2 define the trajectory of the parent particle relative to the primary vertex. If the parent is neutral, this trajectory is simply a straight line which should nominally intersect the primary vertex. However, finite resolution effects in the reconstruction of $\vec{P}$ as well as the positions of P_1 and P_2 imply that the straight line has a finite DCA, b_P, relative to the primary vertex. Real daughter pairs are expected to yield a small b_P values with a finite width PDF $P(b_P)$, whereas combinatorial pairs may have arbitrarily large b_P values. Applying a maximum value selection criterion $b_P \le b_{P,\max}$ is thus in principle useful to further suppress combinatorial pairs. This selection criterion has an efficiency that is determined by the shape and width of the PDF $P(b_P)$. However, be warned that the impact of this selection criterion may be highly correlated to the effects of other selection criteria, so it is typically incorrect to estimate the overall efficiency of the selection criteria as the product of the efficiencies of each of the selection criteria taken separately.

DCA of the Daughter Tracks Relative to the Main Vertex

In very high track multiplicity environments, particularly in the study of relativistic heavy-ion collisions, it is usually effective to also use minimal value selection criteria on the DCA of daughter particles d_+ and d_- relative to the position of the main vertex to suppress the number of combinatorial pairs. Note that while symmetric selection criteria may be reasonable, for instance, for K_s^0 that decay into a pair $\pi^+\pi^-$, asymmetric selection criteria may be better suited for Λ^0 that produce a heavy and a light particle because the heavy particle typically carries a larger fraction of the momentum of the parent (in the lab reference frame) and thus tends to point directly at the main vertex.

Other Selection Criteria

Various backgrounds and instrumental effects may hinder measurements of V^0. Analyses are thus often limited to specific transverse momentum ranges of the daughter particles and the parent. Various track quality selection criteria may also be applied to the daughter particles to minimize contamination by primary particles and fake tracks.

Topological Variable Calculations

Calculation of the DCA between a charged particle track and the primary vertex requires the track be projected near the origin of the track $x = 0$, corresponding to the region of the primary vertex. One can then estimate the DCA based on a nonlinear distance minimization method or use a linear approximation of the track in the vicinity of the primary vertex. Both techniques are briefly outlined in §9.4.

The calculation of the distance between two tracks produces points $\vec{C}_1$, $\vec{C}_2$, and $\vec{P}_2$. The points $\vec{P}_2$ is used in combination with the primary vertex position $\vec{P}_1$ to estimate the path length r_{12} of the parent particle before its decay

$$r_{12} = \left[(\vec{P}_2 - \vec{P}_1) \cdot (\vec{P}_2 - \vec{P}_1)\right]^{1/2}, \tag{8.163}$$

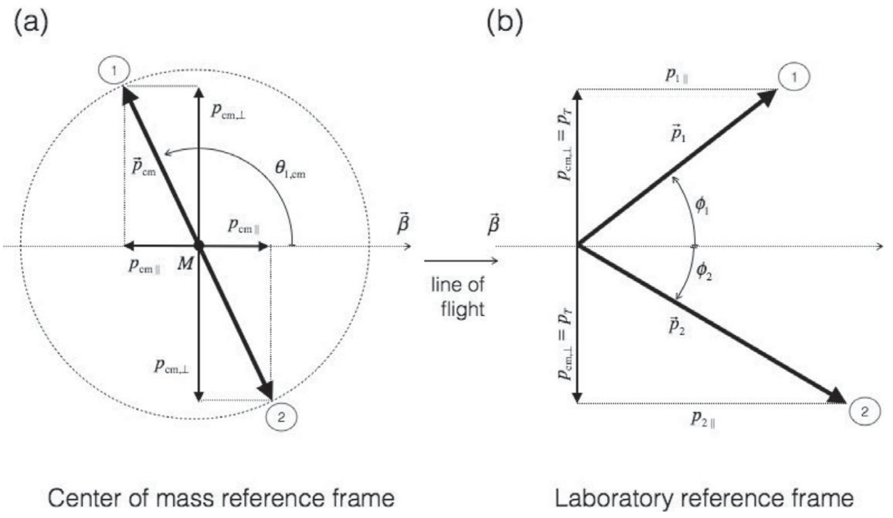

Fig. 8.40 Two-body decay kinematics in (a) the rest frame of parent particle and (b) the laboratory used in the definition of Armenteros–Podolansky variables. The parent particle has a mass *M* and the two daughter particles have masses m_1 and m_2. Note how the momentum components transverse to the line of flight are invariant under a Lorentz boost between the center of mass and laboratory frames.

whereas the points C_1 and C_2 are used to project the tracks and obtain the momentum vectors $\vec{p}_1$ and $\vec{p}_2$ at the decay vertex $\vec{P}_2$. The momentum of the parent particle is thus simply the sum of these two vectors:

$$\vec{P} = \vec{p}_1 + \vec{p}_2. \tag{8.164}$$

It is optionally possible to carry out a constrained refit of the tracks assuming a specific particle decay model (e.g., $K_s^0 \to \pi^+\pi^-$). Techniques to carry out such fits are documented in the literature (§9.3.2) [25, 45, 87, 178] . The fit yields an updated vertex position $\vec{P}_2$ and moments $\vec{p}_1$ and $\vec{p}_2$.

The vector $\vec{P}$ determines an estimate of the parent direction before the decay. Using the position $\vec{P}_2$ and this vector, one can then next determine the impact parameter (or DCA) of the parent at the primary vertex (provided it can be assumed the parent in fact originates from the main vertex of the interaction) using the DCA determination techniques outlined in §9.4.

The Armenteros–Podolansky Plot

In the rest frame of a two-body decay, the locus of points spanned by the momentum vectors of the two daughter particles form a sphere of radius p_{cm} (Figure 8.40):

$$p_{\mathrm{cm}} = \frac{1}{2\sqrt{s}} \left\{ \left[s - (m_1 - m_2)^2 \right] \left[s - (m_1 + m_2)^2 \right] \right\}^{1/2}. \tag{8.165}$$

This sphere becomes an ellipsoid under a boost in the lab frame and must satisfy

$$E_1E_2 - p_1p_2\cos\phi = \sqrt{m_1^2m_2^2 + M^2p_{\rm cm}^2}, \tag{8.166}$$

where E_i and p_i represent the energy and momenta of the two daughter particles in the lab frame and ϕ is the relative angle between their momentum vectors. Unfortunately, the ellipsoidal nature of the decay sphere is not readily apparent from this expression. However, Armenteros and Podolansky figured out that the ellipsoid can be visualized in terms of two variables ε and α calculated based solely on the momentum vectors of the daughter particles. Since the masses of the parent and the two daughter particles determine the magnitude of p^*, the size and position of the ellipse constitute a unique signature of decays that can be used to analyze data and distinguish different decay types. The technique is now known as the Armenteros–Podolansky plot (or often only the Armenteros plot) [153]. The CM momentum $p_{\rm cm}$ of the daughter particles may be decomposed in terms of longitudinal and transverse components:

$$p_{\rm cm}^2 = p_{{\rm cm},\parallel}^2 + p_{\rm cm,T}^2. \tag{8.167}$$

The transverse components are invariant under a boost in the direction of motion of the parent particle. Let $p_{\rm T} = p_{\rm cm,T} = p_{\rm Lab,T}$. By definition of the polar angles ϕ_1 and ϕ_2 shown in Figure 8.40, one has

$$p_{\rm T} = p_1\sin\phi_1 = p_2\sin\phi_2, \tag{8.168}$$

while conservation of momentum implies the momentum of the parent particle, P, satisfies

$$P = p_1\cos\phi_1 + p_2\cos\phi_2. \tag{8.169}$$

Defining $\phi = \phi_1 + \phi_2$, and given $\sin(\phi_1+\phi_2) = \sin\phi_1\cos\phi_2 + \cos\phi_1\sin\phi_2$, one can use the preceding two expressions to obtain

$$p_{\rm T} = \frac{p_1p_2\sin\phi}{P}. \tag{8.170}$$

It is then convenient to define the variable ϵ as

$$\epsilon = \frac{2p_{\rm T}}{P} = \frac{2p_1p_2\sin\phi}{P^2} = \frac{2\sin\phi_1\sin\phi_2}{\sin\phi}. \tag{8.171}$$

However, $p_{\rm T}$ does not uniquely characterize $p_{\rm cm}$, and one thus needs a way to estimate $p_{{\rm cm},\parallel}$. This can be achieved based on the difference $p_{1,\parallel} - p_{2,\parallel}$. It is then convenient to define a variable α according to

$$\alpha = \frac{p_{1,\parallel} - p_{2,\parallel}}{p_{1,\parallel} + p_{2,\parallel}} = \frac{p_{1,\parallel} - p_{2,\parallel}}{P}. \tag{8.172}$$

Given $\sin(\phi_2-\phi_1) = \sin\phi_2\cos\phi_2 - \cos\phi_1\sin\phi_2$, one finds

$$\alpha = \frac{\sin(\phi_2-\phi_1)}{\sin\phi}, \tag{8.173}$$

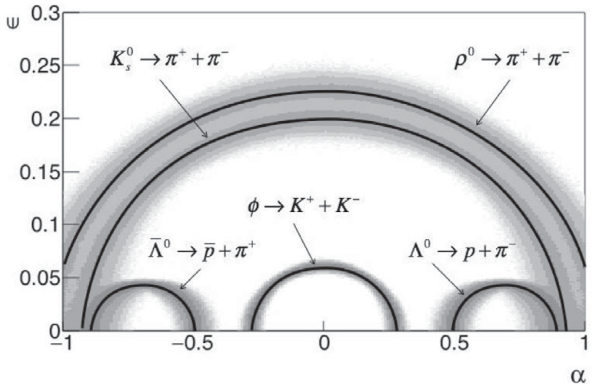

Fig. 8.41 Simulation of an Armenteros–Podolansky plot for selected decays with perfect momentum resolution (solid line) and 3% momentum resolution (shaded scatterplot).

which is uniquely determined by the vectors $\vec{p}_1$, $\vec{p}_2$, and the relative angle ϕ. One can show that the average value of α, noted $\bar{\alpha}$, is equal to (see Problem 8.13 or ref. [153])

$$\bar{\alpha} = \frac{m_1^2 - m_2^2}{M^2} \tag{8.174}$$

and

$$p_{\mathrm{T}}^2 + \frac{1}{4\left(M^{-2} + P^{-2}\right)} \left(p_{1,\parallel} - p_{2,\parallel} - \frac{m_2^2 - m_2^2}{M^2} \right)^2 = p_{\mathrm{cm}}^2. \tag{8.175}$$

This expression may then be rearranged to yield

$$\frac{\epsilon^2}{4\left(p_{\mathrm{cm}}/P\right)^2} + \frac{(\alpha - \bar{\alpha})^2}{4\left[\left(p_{\mathrm{cm}}/M\right)^2 + \left(p_{\mathrm{cm}}/P\right)^2\right]} = 1, \tag{8.176}$$

which is the expression of an ellipse in the α vs. ϵ plane centered at $\alpha = \bar{\alpha}$, $\epsilon = 0$, and with semi-major axes $2\left[\left(p_{\mathrm{cm}}/M\right)^2 + \left(p_{\mathrm{cm}}/P\right)^2\right]^{1/2}$ and $2p_{\mathrm{cm}}/P$, respectively.

The CM momentum p_{cm} and average $\bar{\alpha}$ are determined solely by the masses M, m_1, and m_2. Given that α and ϵ are both determined relative to P, the ellipse is completely specified by and constitutes a unique signature of the decay $M \to m_1 + m_2$.

Figure 8.41 presents examples of ϵ vs. α distributions for selected decays and clearly illustrates the fact that the Armenteros plot is a useful analysis tool for identifying different decaying particles. Indeed, one finds that different decays cover different loci in the ϵ vs. α space and are as such easily recognizable. It is thus rather tempting to use band selection criteria in ϵ vs. α space to select specific decays. One must realize, however, that such selection criteria are strictly equivalent to invariant mass selection criteria. More importantly, such selection criteria cannot distinguish between actual decays and backgrounds caused by instrumental effects. One must then exercise great care in the use of such selection criteria or ideally refrain from their use.

8.6 Searches, Discovery, and Production Limits

Searches for new particles, rare decays, or new particle production processes are an essential component of the work of nuclear and particle physicists. Models designed to explain the structure of matter and fundamental forces, most particularly in searches for physics beyond the standard model of particle physics, abound and predict a vast array of new particles, decay processes, or particle production processes. Not all models can be right, however, and it is in part the role of experimental physicists to test the validity of (credible) model predictions by seeking experimental evidence for the proposed new particles or processes.

8.6.1 Searches for New Particles and Processes

It is fair to say that there are usually more incorrect models than correct ones. So, while many search experiments do identify the particles or processes they seek, many do not. But lack of discovery should not be construed as the failure of an experiment. It should be the models that fail, not the experiments. Search experiments are thus typically designed with great care and attention to detail in order to achieve as high a sensitivity as possible to the sought after particles or processes. The sensitivity of a search is determined by the number of "events" it can examine and its capacity to recognize the sought after phenomenon against background processes. Searches for new particles or low-probability decay modes are typically based on scattering experiments with high-rate capabilities. The idea is to observe as many collisions as possible that are susceptible of producing the predicted new particles or rare decay. This typically requires long data acquisition periods, high beam intensity and target thickness (or luminosity), high granularity and fast detectors capable of handling the large particle production rates and detector occupancy. It usually also requires specialized triggers to select potentially interesting processes, as well as robust and ultrafast data acquisition systems to handle the large throughput of data. Search experiments also usually involve detection redundancy in order to identify and reject background processes.

In the remainder of this section, we first consider the statistical conditions that may justify a claim of discovery and publication in scientific journals. We next discuss how to report the negative findings of experimental searches for new particles or processes.

8.6.2 Discovery: 5σ

Searches for new particles or rare decay processes are largely based on invariant mass reconstruction methods (involving either particles or jets) and require that a sufficiently strong signal (e.g., a peak) be observed relative to background processes. In order to quantify the possibility that an observed peak might be caused by an uninteresting statistical fluctuation, a statistical test must be performed. One formulates the **null hypothesis** that the observed peak or signal might correspond to a background fluctuation. The purpose of the test is thus to assess the probability of this null hypothesis. This requires the choice of a statistic (a test), and one must estimate the **significance level** (p-value) of the observed signal. This corresponds to the probability that given the background rate b from "known" sources, the observed number of events (e.g., in the mass range of interest) would fluctuate up to n_0 or a larger value. A small value of p shows that the data are not compatible with the expected background and suggests that the null hypothesis has an extremely low probability. The observed signal then provides evidence for a new particle (or process).

It is customary in particle physics to convert the value of p into a number of standard deviations σ of a Gaussian distribution, beyond which the one-sided tail has a probability p. Particle physicists typically consider that a new signal or particle can be reported as **discovered** if p is smaller than 3×10^{-7} corresponding to a value of, or in excess of, 5σ (one-sided confidence interval). Note that the correspondence to 5σ is valid only if the signal/background are Gaussian distributed, which is not always the case in practice. The 5σ value is nonetheless useful, though somewhat arbitrary, because it is quite easy to remember. Indeed, no fundamental principle of science or statistics dictates that a 5σ interval (or p-value of 3×10^{-7}) should define a discovery any more than any other "large" $n\sigma$ (small p) value. However, a probability of 3×10^{-7} is construed by most scientists as sufficiently small a value to warrant a claim of discovery, and the "round" number 5 indeed makes it easy to remember. It has thus become the de facto standard requirement in particle and nuclear physics for the announcement of new particle (or signal) discoveries.

This said, many a statistician might question the need for as stringent a requirement as 5σ. Why indeed is 3σ or 4σ not deemed sufficient? As pointed out by Lyons [138], perhaps the most compelling answer to this question is that a number of exciting and interesting "signals" reported at the 3σ or even 4σ level have been later found to disappear once more data were collected. It must also be noted that typical particle/nuclear physics analyses involve many histograms, each with several bins. The chance of one particular bin showing a 5σ effect is thus not that small, let alone a 4σ or 3σ effect. It is also important to note another mitigating factor, the fact that physicists tend to subconsciously make prior assumptions that favor the notion they have discovered something new rather then being in the presence of some undetected procedural or systematic effect(s). While it may not be necessarily equitable or fair to expect both large-purpose experiments (such as the LHC experiments) and smaller, more dedicated experiments to use the same standard, who is to decide which experiment is to apply what standard? Most physicists and journal editors thus prefer abiding by the strict and somewhat arbitrary 5σ rule. However, given that data analyses are often challenged by the use of too small datasets, it is also common to announce and report new signals of weaker significance (e.g., 4.5σ) using a carefully chosen wording (e.g., indication, suggestive evidence, and so on) that properly reflects the status of an observation. However, purported signals observed at less than the 3σ level are typically frowned upon.

The calculation of p-values is often complicated by the existence of nuisance parameters such as uncertainties in the estimated background. Various techniques to handle the calculation of the p-value are discussed in the review article of Lyons [138].

8.6.3 Production Upper Limit

If an experiment is properly designed and operated, a lack of discovery is indeed not a failure, and limits on the production cross section of new particles or branching ratios of nonobserved decays are worth publishing in scientific journals given that they inform models and constrain their predictions. In fact, models can often be rejected altogether by the lack of evidence for the particles or decays they predict.

Negative search results are generally reported in terms of **production limits**. In the search for new particles, such production limits are usually expressed in terms of upper limits on the production cross section of the sought after particle(s), whereas in rare decays, they are most often formulated in terms of an upper limit on the **branching fraction** of the decay process.

Production limits are calculated on the basis of the number of observed events, N_{obs}, as a function of the experimental acceptance and efficiency, ε, for the sought after particle (or process). Determination of the acceptance requires a model of the expected differential cross section ($d\sigma_p/dydp_T$). It is convenient to express the cross section (or branching ratio) of the sought after particle relative to the cross section of a known process, or the number of collisions susceptible of producing the particle or decay. For instance, if the search is conducted on the basis of N–N collisions with a known cross section σ_{NN}, the expected number of observed particles, N_{ex}, may be written

$$N_{\text{ex}} = \mathcal{L} f_{\text{trig}} f_p \sigma_{NN} \varepsilon_p, \tag{8.177}$$

where $\mathcal{L}$ is the integrated luminosity delivered to the experiment; f_{trig} is the fraction of the N–N cross section sampled by the experiment due to trigger selection and efficiency, as well as analysis selection criteria; f_p is the fraction of the cross section (upper limit) that produces the particle of interest; and ε_p is the detection efficiency (of the particle or decay process):

$$\varepsilon_p = \frac{1}{\sigma_p} \int_{\Omega} \varepsilon_p(y, p_T) \frac{d\sigma_p}{dydp_T}, \tag{8.178}$$

where $\varepsilon_p(y, p_T)$ is the particle detection efficiency expressed as a function of rapidity and transverse momentum. So, if the number of observed particles N_{obs} is actually finite, the particle production cross section $\sigma_p = f_p \sigma_{NN}$ can be estimated on the basis of

$$\sigma_p = \frac{N_{\text{obs}}}{\mathcal{L} f_{\text{trig}} \varepsilon_p}. \tag{8.179}$$

For rare decay searches, one replaces $\mathcal{L} f_{\text{trig}}$ by the number of decays produced and observable by the experiment.

If the search produces no candidate particles (or rare decays), one might be tempted to state that the production cross section of the particle vanishes, or that the particle does not exist. But that would be incorrect. Indeed, even if the search uncovers no candidate, it is still conceivable that the particle *does* exist but that its production cross section is too small to be observable in the experiment. Since the production cross section is at best small, it

Table 8.1 Poisson upper limits N_{up} for n observed events

n	CL = 90%	CL = 95%	n	CL = 90%	CL = 95%
0	2.30	3.00	6	10.53	11.84
1	3.89	4.74	7	11.77	13.15
2	5.32	6.30	8	13.00	14.44
3	6.68	7.75	9	14.21	15.71
4	7.99	9.15	10	15.41	16.96
5	9.27	10.51	11	16.60	18.21

Reproduced from R. M. Barnett, et al. Review of particle physics. *Physical Review D*, 54:1–708, 1996.

is legitimate to assume the number of observed particles n can be described by a Poisson distribution:

$$f_P(n|N_{\rm ex}) = \frac{N_{\rm ex}^n e^{-N_{\rm ex}}}{n!}, \tag{8.180}$$

where $N_{\rm ex}$ represents the number of counts that one should expect to find, on average, if the experiment was repeated several times. Since no candidates were found, one seeks the largest value $N_{\rm up}$ compatible with $n = 0$ at a given confidence level (CL). For instance, choosing CL= 10%, one gets

$$f_P(n = 0|N_{\rm ex}) = \frac{(N_{\rm up})^0 e^{-N_{\rm up}}}{0!} = e^{-N_{\rm up}} = 0.1, \tag{8.181}$$

which implies an upper limit $N_{\rm up} = -\ln(0.1) = 2.3$. This value can then be inserted in Eq. (8.179), in lieu of $N_{\rm obs}$, to determine an **upper limit** σ_p for the particle production cross section (or rare decay branching fraction).

If the number of observed candidates n remaining after all selection criteria is not zero but relatively small, it is likely that they correspond to background particles (events) that could not be eliminated by the selection criteria. One must then determine an upper limit $N_{\rm up}$ compatible with the observed background n. Choosing CL, one then has

$$f_P(0 \le k \le n|N_{\rm ex}) = \sum_{k=0}^{n} \frac{(N_{\rm up})^k e^{-N_{\rm up}}}{k!} = \text{CL}, \tag{8.182}$$

which must be solved numerically for $N_{\rm up}$. Table 8.1 lists upper limits $N_{\rm up}$ for small values of n corresponding to the most used confidence levels of 10% and 5%.

Exercises

8.1 Show that in the nonrelativistic limit, $v \approx 0$, the rapidity of a particle, y, is equal to its velocity, $\beta = v/c$.

8.2 Show that the rapidity of particle, defined by Eq. (8.25) transforms according to Eq. (8.27). Hint: Compound two Lorentz transformations and determine the rapidity of the particles.

8.3 Show that for $E \gg m$, the rapidity of a particle, given by Eq. (8.26), may be approximated by the pseudorapidity defined as $\eta = -\ln(\tan(\theta/2))$ (Eq. 8.31).

8.4 Demonstrate Eqs. (8.39) and (8.40) using the definitions of the cosh and sinh functions and the definition (8.26) of the rapidity of a particle.

$$\cosh x = \frac{e^x + e^{-x}}{2}$$
$$\sinh x = \frac{e^x - e^{-x}}{2}$$

8.5 Demonstrate Eqs. (8.41) and (8.42) using the definitions of the cosh and sinh functions (given in the previous problem) and the pseudorapidity of a particle expressed as

$$\eta = \frac{1}{2} \ln \left(\frac{|\vec{p}| + p_z}{|\vec{p}| - p_z} \right).$$

8.6 Consider the TOF slat geometry illustrated in Figure 8.26 and obtain expressions for the velocity of the particle (assuming a flight path L) and its position x along the slat as defined in the figure.

8.7 Verify the expressions (8.41) and (8.42).

8.8 Derive the expression (8.85) for the limits on t for two-body processes.

8.9 Verify the two expressions below by substitution of the values of m_{ij} defined by Eq. (8.158):

$$m_{12}^2 + m_{13}^2 + m_{23}^2 = M^2 + m_1^2 + m_2^2 + m_3^2. \tag{8.159}$$

Additionally demonstrate Eq. (8.160):

$$m_{12}^2 = (P - p_3)^2 = M^2 + m_3^2 - 2ME_3, \tag{8.160}$$

where E_3 is the energy of the third particle in the rest frame of the decaying particle.

8.10 Derive the expression (8.67) for the three-body decay rate.

8.11 Show that the radius of a circle is determined by three points and can be expressed as Eq. (8.108).

8.12 Show that the position resolution achievable with charge sharing between sensors is given by Eq. (8.128).

8.13 Verify the expression (8.174) for the average value of the Armenteros variable α and use this result to demonstrate Eqs. (8.175) and (8.176).